Centrifuge modeling of air sparging — a study of air flow through saturated porous media

Catalina Marulanda [*], Patricia J. Culligan [1], John T. Germaine [2]

Massachusetts Institute of Technology, Room 1-353, 77 Massachusetts Avenue, Cambridge, MA 02139, USA

Abstract

The success of air sparging as a remedial technology for treatment of contaminated aquifers is well documented. However, there is no consensus, to date, on the mechanisms that control the flow of injected air through the saturated ground. Currently, only qualitative results from laboratory experiments are available to predict the zone of influence of a sparging well. Given that the patterns of air flow through the soil will ultimately determine the efficiency of an air sparging treatment, it is important to quantify how sparged air travels through a saturated porous medium. The main objective of this research is to develop a model that describes air transport through saturated porous media. This paper presents results from an ongoing study that employs centrifuge modeling to reproduce in situ air sparging conditions. Centrifuge testing is an experimental technique that allows reduced-scale duplication, in the laboratory, of the stresses and pressure distributions encountered in the field. In situ conditions are critical in the development of actual air flow patterns. Experiments are being conducted in a transparent porous medium consisting of crushed borosilicate glass submerged in fluids of matching indices of refraction. Air is observed as it flows through the porous medium at varying gravitational accelerations. Recorded images of experiments allow the determination of flow patterns, breakthrough velocities, and plume shapes as a function of *g*-level and injection pressure. Results show that air flow patterns vary from fingering, at low *g*-levels, to pulsing at higher accelerations. Grain and pore size distribution of the porous medium do not exclusively control air flow characteristics. Injector geometry has a definite effect on breakthrough velocities and air plume shapes. Experiments have been conducted to compare the velocity of air flow through the saturated porous medium to that of air in pure liquids. Results show that the velocity of air through the medium is lower than that in the pure

[*] Corresponding author. Tel.: +1-617-258-0238; fax: +1-617-253-6044; e-mail: catalina@mit.edu
[1] Tel.: +1-617-258-7093; fax: +1-617-253-6044; e-mail: trishch@mit.edu
[2] Tel.: +1-617-253-7113; fax: +1-617-253-6044; e-mail: jgermain@mit.edu

fluid, as expected. At high *g*-levels however, plume breakthrough velocities are proportional to the velocity of the air in the pure fluid.

1. Introduction

In spite of the success of air sparging as a technique for the cleanup of contaminated soils, there is not, at present, a clear understanding of the manner in which the injected air pathways develop through saturated porous media. Design of air sparging facilities is, in the main, based on results from pilot studies, and on generalized observations from a number of flow visualization studies currently available in the literature. Due to the empirical nature of these observations, they are not always transferable from one site to another.

During air sparging, air is assumed to circulate through the soil either in the form of discrete bubbles or along preferential flow channels. Depending on the existing soil conditions, these two patterns of flow could lead to significantly different zones of influence for the same air sparging well. Given that the efficiency of air sparging treatment is largely based on the extent of the zones of influence of air sparging wells, it is of critical importance to develop a theory that provides more specific information about the factors controlling these zones of influence. The resulting theory can then be translated into guidelines for the design of air sparging systems.

To date, the fundamental mechanisms controlling air flow through porous media are not well understood. Without improved understanding of these mechanisms, the efficient design of air sparging systems is difficult. This paper presents findings of an ongoing research study aimed at investigating the mechanisms controlling air flow through saturated porous media. The objectives of the study are to develop a model that predicts the behavior of injected air in porous media as a function of soil type, soil characteristics, properties of the pore fluid, and injection characteristics.

In order to provide a framework for characterizing flow of air through soils, the literature has been reviewed for background on multiphase flow through porous media, bubble flow in pure liquids, and air flow through tubes, packed beds and fluidized beds. A summary of these topics, in a context relevant to air sparging, is provided in the opening sections of this paper. Next, the principles of centrifuge testing, the experimental technique used in this study to investigate air sparging processes in the laboratory, is described. Finally, the experimental setup and procedures, and an overview of the results obtained to date are presented.

2. Background

2.1. System parameters

Flow of injected air through saturated soils will not occur until the air entry pressure at the injection point is exceeded. The minimum injection pressure needs to be

sufficiently high to overcome the sum of hydrostatic pressure (P_{hyd}) from the column of standing water located above the injection point and capillary pressure (P_{capil}) arising from the presence of the soil. The minimum injection pressure, $(P_{inj})_{min}$, is given by:

$$\left(P_{inj} \right)_{min} = P_{hyd} + P_{capil} = \rho_{pf}\, g h_{wt} + \frac{4\sigma_{g/pf}\cos\theta}{D} \tag{1}$$

in which ρ_{pf} is the density of the pore fluid, h_{wt} is the height of the water table above the sparge point, $\sigma_{g/pf}$ is the interfacial tension between the gas phase and the pore fluid, θ is the contact angle (assumed to be equal to zero for complete wetting), and D is the average pore size diameter.

In addition, air injection pressures must not exceed the in situ effective stress σ', in order to avoid unwanted soil displacements at the sparge point (Widjaja et al. [1]). For a granular material with no tensile strength under Rankine soil conditions, the upper bound to the sparging pressure is given by:

$$\left(P_{inj} \right)_{max} = \min\left(\sigma'_{vertical}, \sigma'_{horizontal} \right)$$

in which

$$\sigma'_{vertical} = \left(\rho_{sat} h_s - \rho_{pf} h_{wt} \right) g$$

and

$$\sigma'_{horizontal} = K_0 \sigma'_{vertical} \tag{2}$$

where ρ_{sat} is the saturated density of the soil and h_s is the height of the soil deposit above the sparge point. The coefficient of earth pressure at rest (K_0) can be estimated from the relationship $K_0 = 1 - \sin\phi'$ (Lambe and Whitman [2]), where ϕ' is the angle of internal friction of the soil, which was an estimated 32° for the experiments reported here.

2.2. Zone of influence of treatment

Knowledge of the extent of the zone affected by the injected air is essential in determining the usefulness of the air sparging treatment technology. In particular, an understanding of the mechanisms controlling patterns of air flow through the soil is necessary to predict the resulting air circulation pathways after injection.

The shape of the zone of influence is usually approximated by either a cone-shaped zone (Nyer and Sutherson [3]) or a by a parabolic shaped zone (Reddy et al. [4], Chen et al. [5]). The dimensions of the zone of influence are believed to depend on soil characteristics, injection rate, and depth of injection.

Lundegard and Andersen [6] found that the zone of influence of an air sparging well varied during the course of injection. Three phases were identified: (1) an expansion phase, characterized by an initial transient period of growth of air pathways in both vertical and horizontal directions; (2) a collapse phase, also transient, during which a reduction of the lateral spread of air pathways occurs; and (3) a steady-state phase, through which the system remains static, provided air injection parameters are kept unchanged. According to the authors, water mounding develops during the expansion

phase, and the zone of influence at this stage is bell-shaped. The zone of influence subsequently decreases and becomes conical as the air reaches the phreatic surface. During the collapse phase, some of the air pathways are re-saturated by ground water and the zone of influence decreases even further.

3. Multiphase flow through porous media

3.1. General background

A comprehensive review of the theory behind multiphase flow is beyond the scope of this paper. This section aims only to highlight a few important aspects of immiscible flow through porous media, that are relevant in following discussions concerning air sparging.

Flow regimes are generally described in terms of dimensionless numbers, which quantify the relative importance of the mechanisms driving and resisting flow. For the case of an interface between two immiscible fluids of interfacial tension σ, advancing with a superficial velocity U along a capillary of equivalent diameter d, the following dimensionless groups have been defined:

$$Re = \frac{\rho U d}{\mu} \text{ — Reynolds number;} \quad Ca = \frac{\mu U}{\sigma} \text{ — Capillary number}$$

$$Bo = \frac{\Delta \rho g d^2}{\sigma} \text{ — Bond number;} \quad We = \frac{\rho U^2 d}{\sigma} \text{ — Weber number.} \tag{3}$$

Re relates inertial forces to viscous forces, Ca relates viscous forces to capillary (surface tension) forces, Bo describes the ratio of gravitational and capillary forces, and We relates inertial forces and capillary forces (Wooding and Morel-Seytoux [7]).

Displacements of immiscible fluids through porous media are controlled by the relative magnitude of buoyancy, viscous and capillary forces (Culligan and Barry [8]). It has been shown, for example, that above a critical Capillary or Bond number capillary trapping of a non-wetting fluid does not occur, whereas below a certain combination of Ca and Bo, trapping is dominated by capillary forces (Ratnam et al. [9]).

The mechanisms at play during air sparging can be well described in terms of dimensionless numbers. Injection of air into the saturated ground involves displacement of a wetting fluid, the interstitial groundwater, by a non-wetting fluid, the injected air. Successful operation of an air sparging well will depend on the extent of invasion of the air front. During injection, capillary forces will tend to entrap the non-wetting phase and therefore to prevent the advancement of the air front. Conversely, buoyancy and viscous forces will act to prevent entrapment. Similar to previous studies of non-aqueous phase liquid (NAPL) flow, the relative influence of capillary, viscous, and buoyancy forces during air sparging can be mapped in a dimensionless Ca–Bo space. Such a map would constitute a phase diagram for air sparging operations, applicable to any system, which

would identify the mechanisms controlling air flow under a wide range of system conditions (Ratnam et al. [9]).

In the context of multiphase flow, dimensionless numbers are conventionally defined in terms of the displacing fluid (Culligan and Barry [8]). In studies of gas–liquid flow however, unless specifically stated, it is general practice to ignore the effect of the gas phase (Grace et al. [10]). The gas–liquid flow convention will be adopted in this study of air sparging, and liquid properties will be used when calculating dimensionless parameters.

The boundaries between linear and non-linear flow through porous media are determined by the magnitude of the Reynolds number. Wright [11] conducted single-phase flow experiments to establish the correlation between turbulence and Reynolds number in the flow of water through granular media. Four flow regimes were identified, coinciding with an increase in the magnitude of the Reynolds number. At low Reynolds numbers, the flow transitions from a laminar regime in which Darcy's law applies, to a non-laminar regime where Darcy's theory is no longer valid and where the type of flow is described as ''steady inertial''. Further increases in flow rate, and hence in the Reynolds number, led to the onset of turbulence in what the author designated as a ''turbulent transition'' regime. At high values of the Reynolds number, the flow finally enters the last regime and becomes fully turbulent.

The boundaries between laminar and turbulent flow in the case of multiphase flow through porous media are not as clearly defined as in the case of single phase transport. Independent dimensionless numbers can be calculated for the various phases, as described by Wooding and Morel-Seytoux [7]. At high flow rates for example, gas–liquid flow through a porous medium can be defined as partially laminar in the gas phase, and fully turbulent in the liquid phase.

3.2. Viscous fingering

Viscous fingers are instabilities that may develop at the point of contact between two fluids, miscible or immiscible, that flow through a porous medium. These instabilities originate due to the contrast in properties between the two fluids at the interface. If differences in density, viscosity and interfacial tension between the two fluids are significant, breakthrough of the displacing fluid will not occur in the form of a uniform invading front. Instead, fingers will develop in the direction of flow, forming intricate branching patterns that bypass significant portions of the medium as they spread (Homsy [12]).

3.2.1. Homogeneous porous media
The first scientist to provide an explanation for the phenomenon of viscous fingering was Hill [13]. He considered the displacement of a fluid of viscosity μ_1 and density ρ_1 by a fluid of viscosity μ_2 and density ρ_2. The change in pressure across the interface (Δp), of a front moving upward with a superficial velocity U through a homogeneous porous medium of intrinsic permeability k, was derived from a one-dimensional form of Darcy's law. If driving forces are greater than stabilizing forces (i.e. $p_2 > p_1$), any small

perturbation of the interface will be amplified and fingers will develop. The condition for unstable *upward* flow is therefore given by the following expression:

$$p_2 - p_1 > 0$$

$$(\rho_1 - \rho_2) g + (\mu_1 - \mu_2) \frac{U}{k} > 0. \tag{4}$$

It is clear from Eq. (4), that depending on the relative magnitude of $\Delta \mu$ and $\Delta \rho$, gravity and viscosity will act as either driving or stabilizing forces. For a given direction of flow a critical velocity U_c can be defined, above which instabilities will amplify (Hill [13]). For the *upward* flow condition described by Eq. (4), this critical velocity is given by:

$$U_c = kg \frac{\rho_2 - \rho_1}{\mu_1 - \mu_2} . \tag{5}$$

Interfacial tension, although not explicitly present in the previous analysis, also has an effect in the mechanisms of formation and propagation of fingers. These mechanisms have been explained in detail by Homsy [12]. It has been observed that after the onset of fingering, a few dominant fingers tend to develop and prevent other smaller, neighboring fingers from further growth. This process is commonly referred to as shielding (Gupta and Greenkorn [14]). The effect of surface tension is effectively to spread these dominant fingers to the extent that they too become fronts, in turn susceptible to fingering. The mechanisms of splitting, shielding and spreading are repeated in the direction of the pressure gradient, until the characteristic fingering patterns are fully developed. Larger interfacial tensions result in wider tip-to-tip finger separations (Homsy [12], Kueper and Frind [15], Pavone [16])

Wettability also has a definite impact on the width of individual fingers. Experiments conducted by Stokes et al. [17] demonstrated that if the displacing fluid preferentially wets the porous medium, then the width of a finger is significantly greater than the effective pore size of the medium, and finger properties can be scaled by the Capillary number. Finger width, specifically, was found to decrease with increasing value of the Capillary number. Conversely, if the displaced fluid preferentially wets the medium, then finger widths were found to be in the same order as pore size, and independent of the Capillary number (Stokes et al. [17]). In the case of non-wetting displacement, shielding tends to dominate over spreading as the fingers develop (Homsy [12]).

Eq. (4) describes the flow conditions that apply during air sparging (i.e. upward flow). Given the low density and the low viscosity of gases, especially relative to typical interstitial pore fluids found in situ, the condition for instability will always be valid during air injection. Fingering should, therefore, always occur as air displaces pore fluid in a porous medium. Furthermore, given that air is non-wetting, it is expected that the scale of the resulting fingers should be of on the order of the pore size.

3.2.2. Heterogeneous porous media

The underlying assumption in the review of fingering phenomena presented in Section 3.2.1, is that the distribution of the hydraulic conductivity of the porous medium is uniform. This assumption is likely to be unrealistic for a natural soil deposit, at least

at the scale of the zone of influence of the sparge well. It is possible in some situations, to sub-divide the porous medium into zones of relatively uniform hydraulic conductivity. The problem becomes determining to which extent each of these zones will control the flow patterns through the medium.

There is a certain degree of controversy in the literature concerning the validity of the term fingering in reference to a heterogeneous porous media. Kueper and Frind [15] state that fingered-like fluid distributions across a heterogeneous medium are the result of channeling, and that they are not ''true'' fingers as defined for the case of a homogeneous media. In a heterogeneous medium, decreases in hydraulic conductivity correspond to decreasing pore size, and ultimately lead to increases in breakthrough pressure. According to the authors, an advancing fluid front will tend to reduce its viscous losses and preferentially invade a layer of lower entry pressure, regardless of the differences between its properties and those of the resident fluid. An invading front will either pond when reaching a fine-grained layer until entry pressure is overcome, or flow laterally until a higher conductivity layer is encountered. Kueper and Frind [15] suggest that ''fingered'' fluid distributions result from this preferential channeling and that they are not caused by instabilities of the flow.

Other investigators have extended the study of fingering phenomena to include flow through heterogeneous porous media, emphasizing that it is the combined action of the hydraulic conductivity differences and of fingering that determines invasion of a given formation (Brock and Err [18], Tan and Homsy [19], Araktingi and Err [20]). When studying flow through a heterogeneous porous media, the scale of the heterogeneity and the degree of connectivity between the different conductivity units will determine the extent to which the flow regime is viscous-dominated or heterogeneity-dominated (Brock and Err [18], Araktingi and Err [20]). When the scale of the heterogeneity is sufficiently large, hydraulic conductivity distributions will dictate flow patterns, regardless of the viscosity and density contrasts between the invading and the resident fluids in the unit. However, within a unit of higher hydraulic conductivity, the fingering mechanisms of spreading, splitting, and shielding take place, essentially as they would in an isolated homogeneous formation. The boundaries of the layer will limit spreading and splitting of the fingers if the range of variations is greater than the finger width (Brock and Err [18], Araktingi and Err [20], Moissis et al. [21])

4. Gas–liquid flow

As was stated in previous sections, the focus of this research study is to quantitatively describe the fundamental mechanisms controlling the flow of air through saturated porous media, in an effort to develop an experimental and theoretical framework for the practice of air sparging. Of particular interest is to determine how the presence of the porous medium affects air flow in comparison to air flow in pure liquids alone. In order to understand the processes at play during gas injection into saturated soils, the literature was first searched for results from injection of gases into pure liquids. The amount of research done on this topic is extensive. In a critical review of the literature on bubble

flow, Ponter and Surati [22] maintain that over 500 papers have been published on this subject over the past three decades.

This section presents only a brief summary of a number of studies on gas–liquid flow, which have been found useful in understanding the mechanisms controlling bubbly flow in pure fluids. Although these mechanisms may not directly apply to flow of air through porous media, they provide useful information on the basic behavior of gas–liquid flow. This section also includes a review of gas–liquid flow through fluidized and packed beds, as well as a very brief summary of the flow of foam through porous media.

4.1. Movement of air bubbles in pure fluids

4.1.1. The formation of bubbles

The formation of a bubble at an orifice depends on factors such as orifice geometry, flow rate, air pressure, and characteristics of the fluid media. This section summarizes results from investigations conducted on bubbles formed from upward-facing orifices of circular cross-section. Experiments reported here were always conducted in sufficiently large cylinders such that wall-effects did not significantly affect the motion of bubbles.

Three stages that have been identified as a bubble is formed at an orifice. Under laminar flow conditions, the frequency of bubble emission is proportional to flow rate. Bubbles are relatively uniform, and their size is a function of orifice diameter, surface tension, and fluid density (van Krevelen and Hoftijzer [23], Hughes et al. [24], Davidson and Amick [25], Leibson et al. [26]). As a bubble forms, viscous drag forces accelerate the surrounding fluid. The bubble is necked by the circulating fluid and detaches from the orifice due to a combination of buoyancy and fluid motion. The bubble rises in the fluid due to buoyancy forces, and the portion of it left behind at the orifice becomes the nucleus for the next bubble. As the flow rate is increased and turbulent flow conditions are reached, the bubble diameter increases, and the bubble shape becomes irregular and nonuniform. Bubble coalescence occurs very close to the orifice and the resultant bubble only rises a small distance before it shatters into many small bubbles. As the flow rate is increased further, the large bubbles undergo a second coalescence during their ascent, and the gas appears to come out of the orifice as one continuous jet. In reality, irregular bubbles are rising with a very rapid swirling motion. Fluid circulates in a large eddy near the orifice, shattering the large bubbles and forming a large number of very fine bubbles (Davidson and Amick [25], Leibson et al. [26]). Fig. 1 shows a sequence of pictures taken during centrifuge testing of glycerol in which bubble coalescence is observed.

4.1.2. Single bubbles

The movement of a single bubble in an infinite fluid medium is not simple to establish because the properties of the bubble change continuously along its trajectory. The shape of the bubble, and therefore its velocity, will be primarily determined by the interaction between buoyancy, viscosity and interfacial tension.

Haberman and Morton [27] conducted an extensive study on the motion of single bubbles in various fluids. Results showed that the shape of rising bubbles changes as
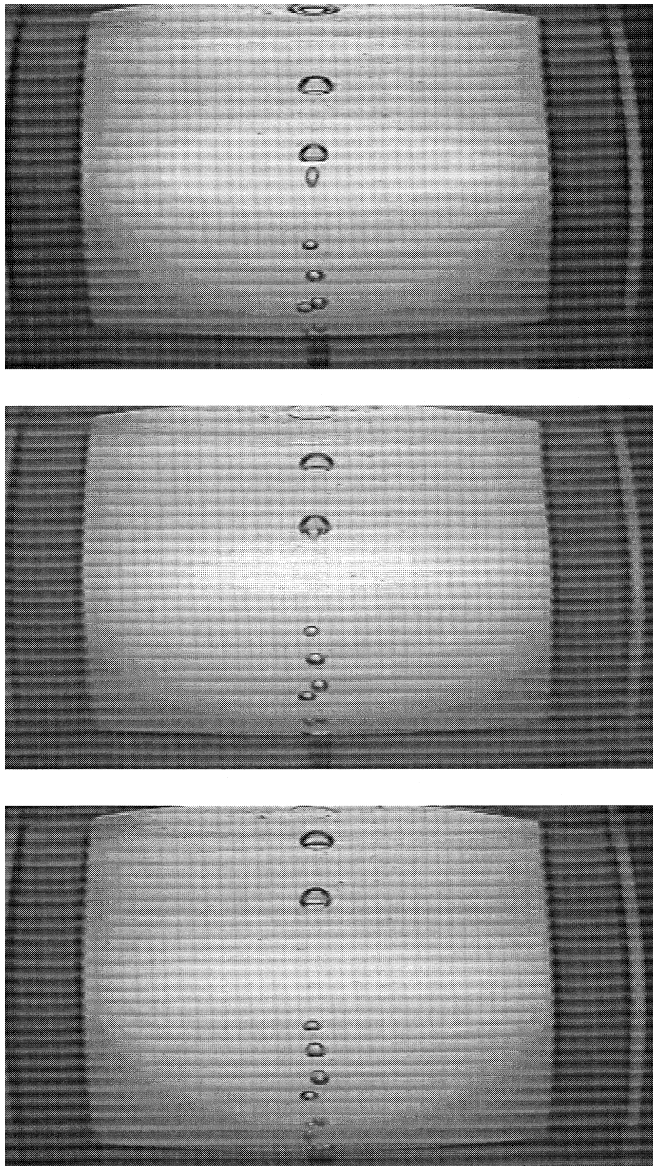
Fig. 1. Sequence of bubble coalescence.

their size increases. Bubbles are initially spherical, become ellipsoidal as they grow, and finally develop into large bubbles known as spherical caps, that have a mushroom-like shape. The specific bubble volume at which these transitions occur depends on the characteristic properties of the surrounding fluid. Observations also showed that the velocity of bubbles is dependent on size. Larger bubbles rise at higher velocities than

smaller ones, and their shape changes during ascent. Haberman and Morton [27] evaluated the drag coefficients of rising bubbles, to try to interpret their changes in velocity. The authors found that the drag coefficients acting on these bubbles are predicted, at low velocities, by Stokes' law, while at higher velocities they are predicted by the Hadamard–Rybczynsky law.

Stokes' law estimates the drag coefficient on a rigid spherical particle moving relative to a fluid of infinite extent. In the context of bubble flow, a rigid body designates a bubble in which no circulation of inner-gas occurs during ascent. At low Reynolds numbers, the terminal rise velocity (v_∞) of small single bubbles predicted using Stokes' law is given by:

$$v_\infty = \frac{1}{18} \frac{d^2 g (\rho_f - \rho_g)}{\mu_f} \tag{6}$$

in which d is the diameter of the bubble, ρ_f and ρ_g are the densities of the fluid and the gas, respectively, and μ_f is the viscosity of the fluid (Wallis [28]). Analogously, the Hadamard–Rybczynski law estimates the drag coefficient of a fluid sphere. A fluid sphere designates, in this case, a bubble within which gas is circulating during ascent. For cases in which $\mu_g \ll \mu_f$, the terminal rise velocity of a such a sphere predicted by this law is (Wallis [28], Clift et al. [29]):

$$v_\infty = \frac{d^2 g (\rho_f - \rho_g)}{12 \mu_f}. \tag{7}$$

As noted, Haberman and Morton [27] found that below a certain size the terminal rise velocity of bubbles in liquids is well predicted by Stokes' law. However, above a critical diameter, bubble velocity is better described by the Hadamard–Rybczynski law, which gives velocities approximately 50% higher than those estimated by Stokes' law. The value of this critical diameter also depends on the properties of the fluid. Based on their observations, Haberman and Morton suggested that small bubbles rising in liquids behave as rigid bodies. As the size of the bubbles increases, the onset of internal circulation leads to a decrease in the drag coefficient, which ultimately results in an increase in the rise velocity. Larger bubbles therefore behave as fluid bodies.

In an ideal system, i.e. one exempt of all contamination, the rise velocity of all bubbles, regardless of their size, is described by the Hadamard–Rybczynski law. However, unless extreme precautions are taken, surface-active contaminants are typically present in any system. These contaminants tend to accumulate at the interface between two fluids, resulting in a reduction of the interfacial tension (Clift et al. [29]). As bubbles rise in liquids, surface-active contaminants tend to be swept to the rear, causing gradients in interfacial tension across the surface of the bubble. These gradients result in tangential stresses, which ultimately lead to decreases in bubble velocity. Smaller bubbles are more susceptible to these gradients than larger bubbles, and therefore their velocities are lower than those of larger bubbles (Levich [30]). The motion of small bubbles in contaminated systems is thus described by Stokes' law rather than Hadamard–Rybczynski's law.

As mentioned previously, three types of bubble shapes exist: small bubbles are spherical, larger bubbles are flattened and have a predominantly ellipsoidal shape, and the largest bubbles are called spherical caps (mushroom cap shape). The motion of these bubbles changes according to their size, alternating from rectilinear, to helical path, to rectilinear with rocking (Haberman and Morton [27]). Fig. 2, taken from Haberman and Morton's paper, shows the evolution of bubble velocity and shape as a function of their diameter.

The work of Haberman and Morton [27] has been greatly extended over the years. A large data base exists in the literature of bubbles sizes and their corresponding velocities in a variety of fluids. The work of Grace et al. [10], for example, provides a graphical method of estimating terminal velocities of bubbles for all types of flow regimes. Analytical expressions have also been derived for various types of bubble sizes and fluid properties. The reader is referred to Wegener and Parlange [31], Wallis [32], and Comolet [33,34] for a complete treatment of the subject.

4.2. Gas–liquid flow in vertical tubes

The study of gas flow in pure liquids only helps to provide information on the general behavior of bubbles in liquids. This behavior, however, is likely to be drastically
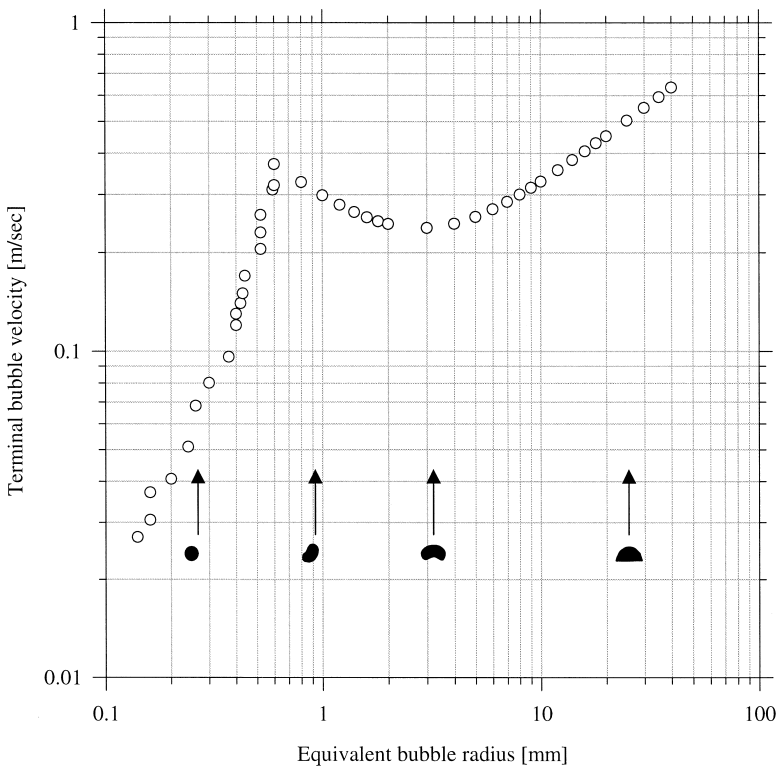

Fig. 2. Bubble velocity vs. equivalent radius.

different when the flow of gas is restricted to the interconnected channels of a porous medium. In an initial attempt to describe gas flow through porous media, studies on flow of gases in saturated vertical tubes were reviewed.

Taitel et al. [35] studied gas–liquid flow in vertical tubes and described conditions in which transitions between flow patterns occur as gas flow rate is varied. Four distinct modes of flow are identified: (1) bubble flow, where discrete bubbles are distributed in a liquid phase; (2) slug flow, in which large bullet-shaped bubbles of diameters similar to those of the tube move uniformly, separated by slugs of liquid; (3) churn flow, in which the large bubbles become distorted and the liquid slugs collapse due to a high gas concentration; and (4) annular flow, where the gas phase is continuous along the tube. Annular flow is characterized by a liquid film flowing adjacent to the wall and a gas core which carries entrained gas droplets. Fig. 3 shows a schematic of the various patterns of gas flow through a pipe. These same patterns of flow were also observed by Mishima and Hibiki [36] in their study of gas–liquid flow through vertical capillary tubes.

As the gas rate flowing into a tube is increased, bubble density increases and coalescence occurs. With increasing flow rates the rate of coalescence increases but, as explained in the study of bubble flow in free liquids, with the onset of turbulence bubbles start to shatter, leading to a large number of small bubbles. If the coalescence rate is higher than the rate at which bubbles break up, a transition to slug flow takes place. As the flow rate is further increased transitions to churn and annular flow occur (Taitel et al. [35]). In a study of gas–liquid flow through artificially fabricated fractures, Fourar and Bories [37] observed patterns of flow consistent with those observed by

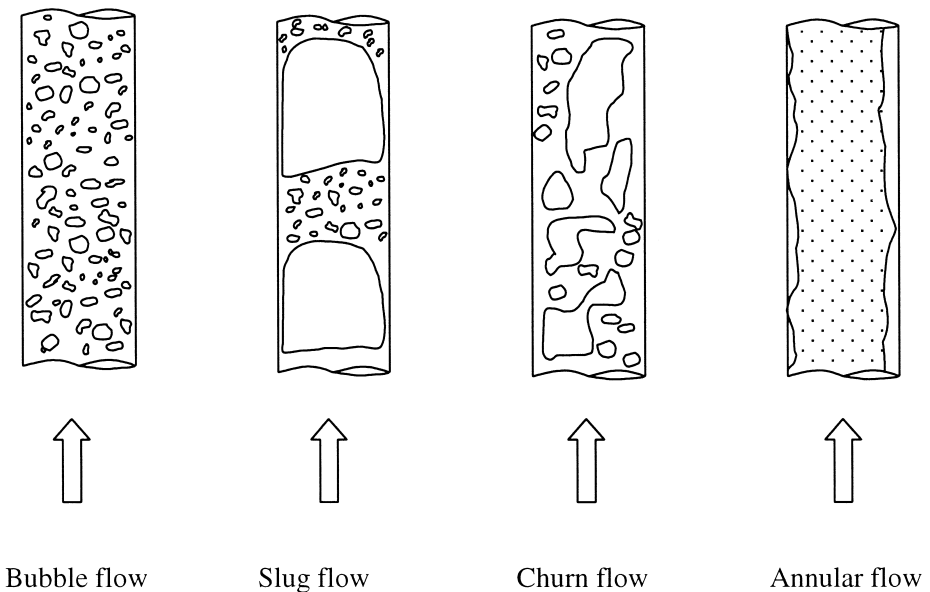Bubble flow   Slug flow   Churn flow   Annular flow

Fig. 3. Flow regimes in vertical tubes.

Taitel et al. [35]. However, at relatively low values of flow rate, Fourar and Bories [37] observed what was referred to as fingering bubble flow. The flow patterns obtained showed more similarity to those observed in tubes than those expected in porous media.

4.3. Gas–liquid flow in fluidized beds and packed beds

Even though gas flow in tubes is a highly idealized and simplified model for air flow through porous media, it provides valuable information on how restrictions affect the general patterns of air flow, relative to the flow in pure liquids. The network of void spaces in a porous medium however, is significantly more complex than that in a tube, and therefore variations in the flow patterns described by Taitel et al. [35] are to be expected. One step closer to the study of air flow through ''real'' porous media can be taken by reviewing the work conducted on gas–liquid flow through fluidized and packed beds.

A fluidized bed is a bed of particles that can be partly or fully supported by an upward flow of fluid through its void spaces (Davidson et al. [38]). When air is injected into a fluidized bed, bubbles are formed in the same manner as when air is injected into a pure liquid. Bubbles formed in fluidized beds are similar to spherical caps rising in pure liquids, but their shape depends on the nature of the particles in the bed (Davidson et al. [38]). Experimental results show that the rise velocity of bubbles in fluidized beds is lower than that in pure liquids, and that it decreases with increasing soil particle density. However, a point is reached at which for a given bubble diameter and a given solid concentration, the soil particles have no effect on the rise velocity of the bubbles (Tsuchiya et al. [39], Bly and Worden [40], Tsuchiya and Furumoto [41]). Experiments conducted by Tsuchiya and Furumoto [41] evaluated the influence of particle density, particle shape and bubble size on the resulting velocity and degree of tortuosity of rising bubbles. The authors found that high particle densities in fluidized beds account for a ''general'' reduction in the observed velocity of bubbles of all sizes, independently of the shape of the particles in the bed. This effect was found to be more pronounced for smaller bubbles. However, according to Tsuchiya and Furumoto [41], there is a ''peculiar'' reduction in observed bubble rise velocities (for moderate and high solid densities) that depends strongly on both bubble size and particle shape. This latter effect is also particularly evident in the rise velocity and degree of tortuosity of small bubbles rising in beds of irregular sand particles. Velocities of small bubbles through the sand bed decreased greatly when compared to those in a pure fluid or through a bed of spherical glass beads. Rising paths of small bubbles through the sand bed were also highly tortuous. Rise velocities of larger bubbles were less affected by particle shape, and their rising paths were less tortuous.

It is important to emphasize that injection flow rates in fluidized beds are kept relatively low in order to maintain bubble flow conditions during operation, since the objective of the system is to enhance exchange between the solid and the fluid phases. High flow rates would lead to bubble coalescence and ultimately to the formation of air jets, therefore decreasing the efficiency of the system. Even though restrictions to air flow exist in fluidized beds relative to pure fluid systems, the boundaries restricting air flow are not as fixed as in the case of a porous media. Therefore, it is reasonable to

assume that the presence of solid particles in fluidized beds is less disruptive to the rising motion of large bubbles. Large bubbles exert greater buoyancy and inertial forces than small bubbles, and therefore can potentially displace suspended solid particles encountered in their trajectory.

The study of air flow through packed beds has also provided some insight in the study of gas flow through porous media. As opposed to fluidized beds, packed beds usually consist of columns of small diameters packed with a given porous material, through which the flow is heavily restricted. Continuous gas and liquid flow take place simultaneously through the columns. Observations of gas flow regimes in tubes made by Taitel et al. [35], are remarkably similar to those made in packed beds by Turpin and Huntingdon [42]. The authors identify three separate regimes of gas flow, starting with bubbly flow at low gas flow rates. As the gas flow rate is increased at a constant liquid flow rate, the onset of slug flow is observed. Slug flow is defined as a non-homogeneous flow regime characterized by alternate portions of gas and liquid passing through the column. With further increases in flow rate ''spray flow'' begins, described as a continuous gas flow regime in which the liquid is suspended as a mist in the gas stream. Weekman and Myers [43] had conducted similar experiments, and also identified three regimes of flow depending on input gas flow rate. Although not totally consistent with observations of Turpin and Huntingdon [42], Weekman and Myers [43] described a transgression of flow regimes with increasing flow rate from a continuous gas flow, to rippling flow, to pulsing flow.

4.4. Foams in porous media

Only a very brief discussion on the influence of porous media on the characteristics of foam is presented in this section. The generation of foam within the void space of a porous medium is believed to provide insight in the mechanisms of bubble formation.

Formation of foam bubbles in packs of granular soils by simultaneous circulation of aqueous surfactant solutions and gas has shown that the average size of foam bubbles exiting a porous medium is independent of the bubble size of the foam injected into the medium. When the size of injected bubbles is greater than pore size, bubbles are subjected to splitting at branch points in the pore structure. Breakup of bubbles and dispersion of fluids continues along the bed until a ''limiting'' size is reached. Conversely, if the size of the foam bubbles injected into the porous media is smaller than the particle size of the medium, bubble coalescence occurs, ultimately yielding to larger foam bubbles (Gido et al. [44]; Nutt et al. [45]). Nutt et al. [45] further suggest that the size of the foam bubbles exiting a given porous medium is approximately equal to the average pore size of the medium.

5. Air injection in saturated porous media: experimental studies on air flow patterns

Few studies are available in the literature that investigate the flow of air through soils during air sparging. The most complete series of visualization tests available were

conducted by Ji et al. [46] in their study of air flow patterns through water saturated glass beads. Beads of various sizes were used in their experiments, in an effort to determine the influence of porous media characteristics on air plume behavior and shape. Results showed that bubbly flow developed through the coarser-grained packs of beads (4 mm in diameter), while channeling flow was observed through the finer-grained material (0.75 mm in diameter). Observations from studies conducted by Wehrle [47] and Semer et al. [48] on air flow through granular soils are consistent with results presented by Ji et al. [46]. Both studies reported bubbly flow conditions taking place in gravel formations following air injection. Wehrle [47] indicated that injected air rose through the gravel in the form of ''groups of pulsating bubbles'', and that no flow occurred through the sand. Semer et al. [48] reported bubbly flow through the gravel, and injected air flowed along preferential flow pathways through the sand.

No definite conclusion has therefore been reached on the grain-size at which transition between bubbly and channeling flow occurs in porous media. Authors have loosely referred to coarser and finer materials, but in a context relative to the specific experiments being conducted. Moreover, as will be discussed in a following section, laboratory visualization experiments do not accurately reproduce the stresses acting at the injection point of an air sparging well, and this may lead to inaccurate modeling of
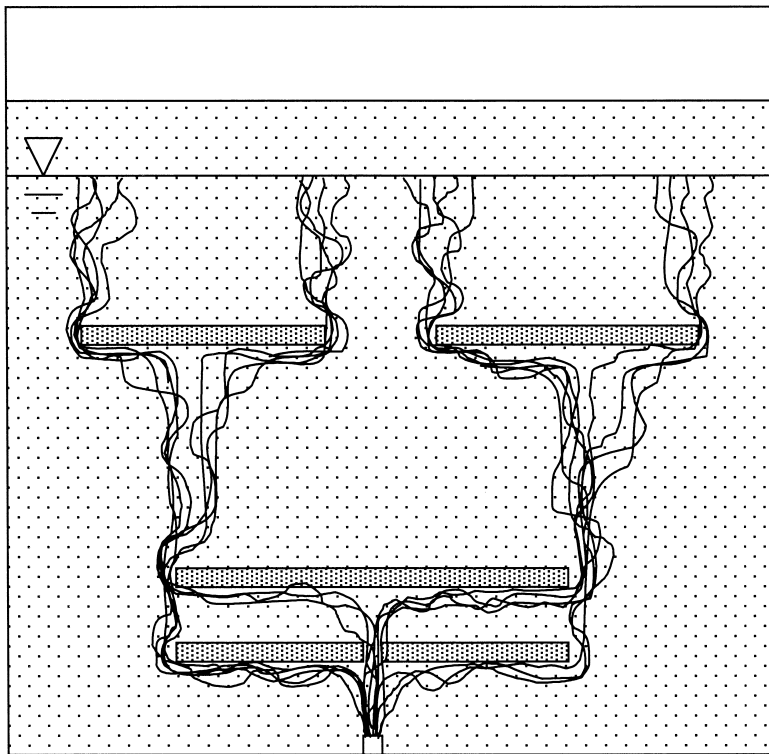

Fig. 4. Schematic of air flow through heterogeneous porous media.

flow conditions in the laboratory. Flow regimes are clearly difficult to observe during in situ air injection, which further limits the amount of information available.

Laboratory simulations of air sparging, nonetheless, have resulted in a consistent observation regarding patterns of air flow, namely that the presence of large-scale heterogeneities completely disrupts the flow pathways through the soil. Results presented by Ji et al. [46] and Baker and Benson [49] show that vertical air flow is prevented by layers of low hydraulic conductivity, which force the flow to spread horizontally until the layer of finer material is bypassed. A schematic of air flow patterns through heterogeneous porous media is shown on Fig. 4. Results from field tests are also consistent with this behavior, as indicated for example by Reddy et al. [4], Bohler et al. [50], and Marley et al. [51].

6. Centrifuge modeling of air sparging

The objective of this study is to conduct a fundamental investigation on air-flow patterns during air sparging in saturated porous media. The experimental technique employed for this investigation is that of geotechnical centrifuge modeling. The principles of centrifuge modeling are outlined in the following sections.

6.1. Overview of geotechnical centrifuge testing

Over the past decade, the use of centrifuge modeling in environmental applications has gained increasing acceptance, as contaminant transport processes have been successfully modeled using this technique (Arulanandan et al. [52], Hensley and Savvidou [53]). Centrifuge modeling offers the unique advantage of testing, in the laboratory, the same material encountered in the field, under the exact same stress and fluid pressure conditions that exist in situ. In a field such as geotechnical engineering, in which both mechanical and hydraulic properties of soils are controlled by the state of stress of the material, the ability to reproduce field stresses is critical (Taylor [54]).

The principles behind centrifuge testing are as follows: the behavior of a prototype subjected to the earth's gravity g, can be reproduced in the laboratory by a scaled model subjected to a centrifugal force ng. The dimensions of the model need to be scaled down by a factor of $1/n$ as shown in Fig. 5. Stress distributions throughout the model and the prototype are the same, as long as the product of depth times acceleration for model and prototype are identical (Hensley and Savvidou [53]). In the specific case of air sparging for example, if Eqs. (1) and (2), which refer to prototype (field-scale) conditions, are re-written for the centrifuge model, they become:

$$\left(P_{\text{inj}}\right)_{\text{min}}\big|_{\text{model}} = P_{\text{hyd}} + P_{\text{capil}} = \rho_{\text{pf}} ng \frac{h_{\text{wt}}}{n} + \frac{4\sigma_{\text{g}/\text{pf}}\cos\theta}{D} \tag{8}$$

and

$$\left(P_{\text{inj}}\right)_{\text{max}}\big|_{\text{model}} = K_0\left(\rho_{\text{sat}}\frac{h_{\text{s}}}{n} - \rho_{\text{pf}}\frac{h_{\text{wt}}}{n}\right)ng. \tag{9}$$
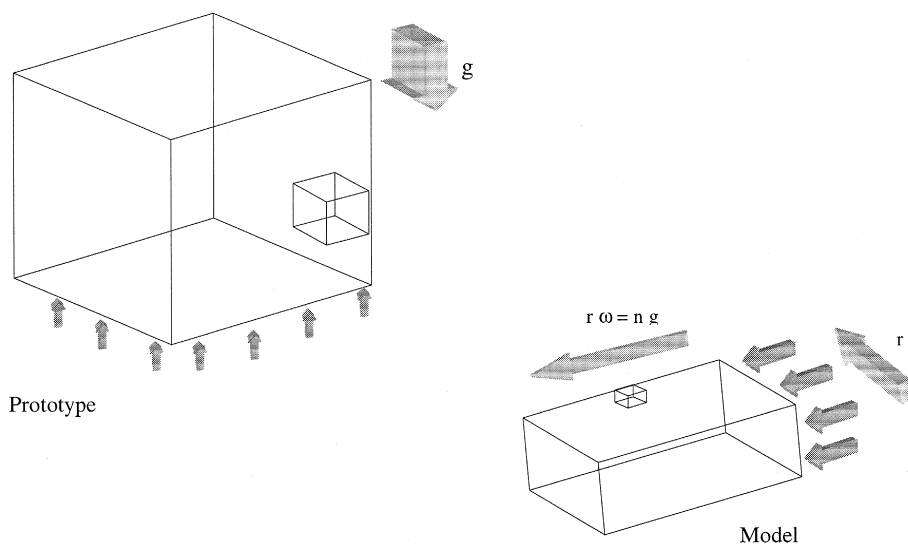
Fig. 5. Principles of centrifuge modeling.

Therefore, centrifuge testing is a technique through which in situ stress and fluid pressure distributions can be realistically reproduced at a reduced scale in the laboratory. This ensures that the modeled values of air entry pressure, hydrostatic pressure, and hydraulic conductivity are representative of the prototype problem. No other experimental method, outside full-scale testing, offers the same advantages as centrifuge testing in this respect.

In general, centrifuge modeling requires that scaling laws be derived for the specific type of experiments conducted. Scaling laws relate the variables measured in the model (i.e. velocities, time for breakthrough) to the actual processes occurring in the prototype. No scaling laws have been derived for the data presented in this paper. This is because the results of the experiments reported here have been aimed at understanding the fundamental mechanisms controlling transport of air through saturated media, and were not intended to model the behavior of any specific air sparging prototype. It is the belief of the authors, that until the interactions between buoyancy and capillary forces during flow of air through saturated soils are fully understood, a complete model of air sparging cannot be proposed.

The influence of the soil particle size during centrifuge testing is an issue that has received considerable attention from the modeling community. In particular, the need to reduce the size of soil particles by a factor n, corresponding to the centrifugal acceleration to which the model is subjected, has been considered (Taylor [54]). However, it is accepted that since the behavior of soil particles is not exclusively dictated by their size but is also influenced by their mechanical and surface properties (i.e., stress–strain behavior, surface–pore fluid interactions), the effects of particle size are not significant in all cases (Taylor [54]). In the specific case of air sparging, surface particle effects typically observed in clays can be ignored, since this technology will

ordinarily not be used for cleanup of clayey deposits. Particle effects could, indeed, be significant during centrifuge modeling if, as discussed by Taylor [54], the operation of an air sparging well on a very coarse granular deposit was being modeled at high centrifugal accelerations. In such a case, soil particle size could be significant relative to model dimensions, and variations between the behavior of model and prototype would be expected. These are not the conditions reproduced by the experiments presented in this paper, and therefore scaling of soil particles was not performed on the results presented. It is believed that air flow patterns are mainly controlled by pressure distributions and force balances acting on the soil–pore fluid system as a whole, rather than by effects at the level of individual particles.

In summary, an important distinction needs to be made before any discussion on results from centrifuge tests is presented. Air flow through saturated porous media will not be affected by particle size effects due to *scaling* of dimensions during centrifuge testing. However, within the range of particle sizes which is small relative to model dimensions, particle size will have a drastic effect on air flow, as discussed in Section 5 (i.e. sample heterogeneity).

6.2. Centrifuge study of governing mechanisms

Centrifuge testing offers the unique advantage of conducting experiments under increasingly higher injection pressures, while maintaining the overall stability of the system. As shown by Eq. (8) the value of the minimum injection pressure increases as a function of g-level. Air flow patterns under a wide range of injection pressures and air flow rates can be investigated directly, without exceeding the maximum pressure requirements imposed by Eq. (9). Some investigators have suggested that increasing air injection pressure increases air channel density and air saturation (Marley et al. [51], Ahfeld et al. [55], Brown [56]). Others have maintained that after an initial increase in air saturation, increasing injection pressure does not result in significantly higher saturations (Baker and Benson [49]). It is likely that the laboratory experiments in which the effect of higher injection pressures on air flow patterns has been investigated, have caused fracturing of soil samples, as the injection pressures exceed in situ effective stresses. Ji et al. [46] for example, report ''fluidization'' of their porous media as air injection pressure is increased beyond the critical value. If an injection pressure gradient (ΔP) is defined as:

$$\Delta P = P_{\text{inj}} - \rho_{pf} ng \frac{h_{\text{wt}}}{n} \tag{10}$$

then the effect of increasing injection flow rate can also be evaluated over a wider range than what would be possible in reduced-scale experiments conducted at $1 \times g$ in the laboratory. It is very likely that air flow regimes vary significantly as air flow rates through the soil increase, as was the case for flow of air in pure liquids.

The fundamental processes that occur during flow of air through porous media can also be studied through centrifuge testing. The Bond number for example, defined for the prototype scale by Eq. (3), can be re-written for the centrifuge model as:

$$Bo|_{\text{model}} = \frac{\Delta \rho ngd^2}{\sigma}. \tag{11}$$

Therefore, the effect of buoyancy on flow patterns of air through soils can be investigated during centrifuge testing, by observing the behavior of a given centrifuge model subjected to a range of centrifugal accelerations. The relationship between displacing and entrapping forces in the medium, and their effect on observed flow regimes, can thus be easily established using this technique. No other experimental technique offers the same flexibility as centrifuge modeling in this respect.

7. Experimental methods

7.1. Porous medium

One of the central objectives of this study was to observe and characterize air flow patterns during air sparging experiments. In order to visualize the flow of air through the soil, a transparent porous medium was developed. This was accomplished using the *immersion method* described by Wakabayashi [57]. The principle behind this method is that a solid particle submerged in a fluid of matching index of refraction becomes transparent when exposed to a light within a certain range of wavelengths. This principle has been used by a number of investigators over the years (Dantu [58], Rangelow et al. [59], Konagai et al. [60], Montemagno and Gray [61]).

Results from preliminary tests, suggested that borosilicate glass had refractive properties that could be matched by commercially available fluids, and therefore it was chosen as a substitute for soil particles. The material was purchased in bulk and manually crushed in the laboratory using a compaction hammer. Better results were obtained using crushed glass rods than beads, most likely due to the higher purity of the rods (Konagai et al. [60]). The crushed material was subsequently washed, dried, and sieved in order to separate it into adequate grain-sizes.

Two grain-size distributions have been used to date in air sparging experiments, namely a medium-grained material with an effective grain-size diameter $D_{10} = 0.8$ mm, and a fine-grained material with $D_{10} = 0.077$ mm. Grain-size distributions are shown in Fig. 6. As seen in the figure, both solid fractions are fairly uniform. Visual inspection of the coarser particles reveals that they are fairly angular. The specific gravity (G_s) of the glass was measured and found to be equal to 2.24.

7.2. Pore fluid

The refractive index, n, of borosilicate glass, as measured by a commercial laboratory, is 1.4716. Two fluids have been used in the experiments that match this value of n, namely glycerol and a fused silica liquid (immersion liquid). The immersion liquid, made to specification from R.P. Cargille Laboratories, was ordered to exactly match the index of refraction of the glass. Both fluids are transparent, non-toxic and non-volatile. Characteristic properties of both liquids are summarized in Table 1. The properties of water are also provided for reference. It is evident from the values presented in the table,
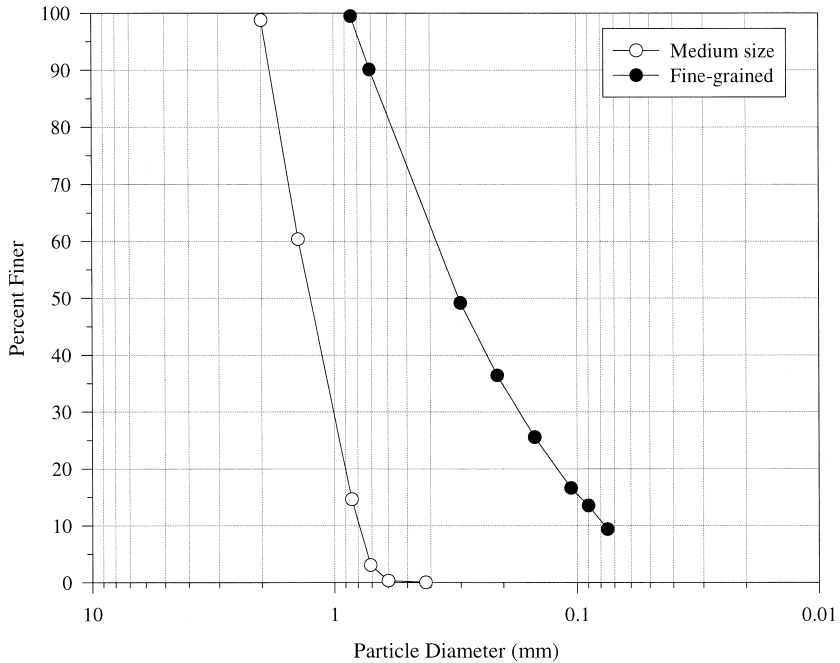
Fig. 6. Grain-size distribution of porous materials used.

that the properties of the fluids used are significantly different than those of water, the pore fluid typically found in situ. However, as discussed in Section 3.1, the use of dimensionless numbers in the evaluation of air flow through porous media accounts for widely different fluid properties. Since it is the relative magnitude of viscous, buoyant and capillary forces which controls flow, and since these forces can be defined independently of the fluid, tests conducted in glycerol and immersion fluid can be used to infer the behavior of an air sparging system in water.

7.3. Experimental setup

All experiments discussed in this paper were conducted using the balanced arm geotechnical centrifuge facility in the Department of Civil and Environmental Engineering at the Massachusetts Institute of Technology (MIT). The MIT centrifuge, a Genisco Model 1231 G-Accelerator, with a load capacity of $13,620 \times g$ kg, can be accelerated

Table 1
Properties of fluids used in air sparging experiments

Fluid type	Index of refraction, n	Kinematic viscosity, ν [cSt]	Density, ρ [g/cm^3]	Interfacial tension, σ [N/m]
Glycerol	1.4714	550	1260	6.3×10^{-2}
Immersion liquid	1.4716	21	850	3.0×10^{-2}
Water	–	1	1000	7.3×10^{-2}

from 0 to $200 \times g$ (0 to 400 rpm). The centrifuge is equipped with a 2.74-m long rotating arm holding two swinging platforms as shown in Fig. 7. A complete description of this facility is provided by Pahwa [62].

All air sparging experiments reported here were conducted in a transparent Plexiglas strong-box of internal dimensions $30 \times 28 \times 10$ cm. After preparing the sample, the box was bolted onto one of the centrifuge swinging platforms. A fluorescent light source was located behind the strong box, which facilitated visual inspection of the sample during each test. Under the strong fluorescent light the saturated medium appeared transparent and the plume of injected air was seen as a black shadow. A miniature wide-angle video camera was also bolted to the platform, directly in front of the box, with which a continuous record of all experiments was obtained. Please refer to Fig. 8 for a diagram of the experimental setup.

Air was supplied to the box from a compressed nitrogen cylinder located on the opposite side of the rotating arm. All tests presented in this paper were conducted at constant injection pressures, that were fractionally above the minimum required entry pressure for the system. Minimum air entry pressure was determined from Eq. (8), and the injection pressure was set prior to the experiment. Two 30-psi pressure transducers were positioned along the pressure line, one near the nitrogen tank and the second one at the entrance of the sample box, as shown in Fig. 7. These transducers provided continuous measurements of the hydrostatic pressure at the bottom of the test box prior to injection, as well as of the injection pressure at two different locations along the

1. Motor
2. Shaft
3. Rotating arm
4. Balancing platform
5. Air cylinder
6. Air sparging sample
7. Electrical connections
8. Lights
9. Central camera
10. Electronic valve
11. Pressure regulator
12. Pressure transducer
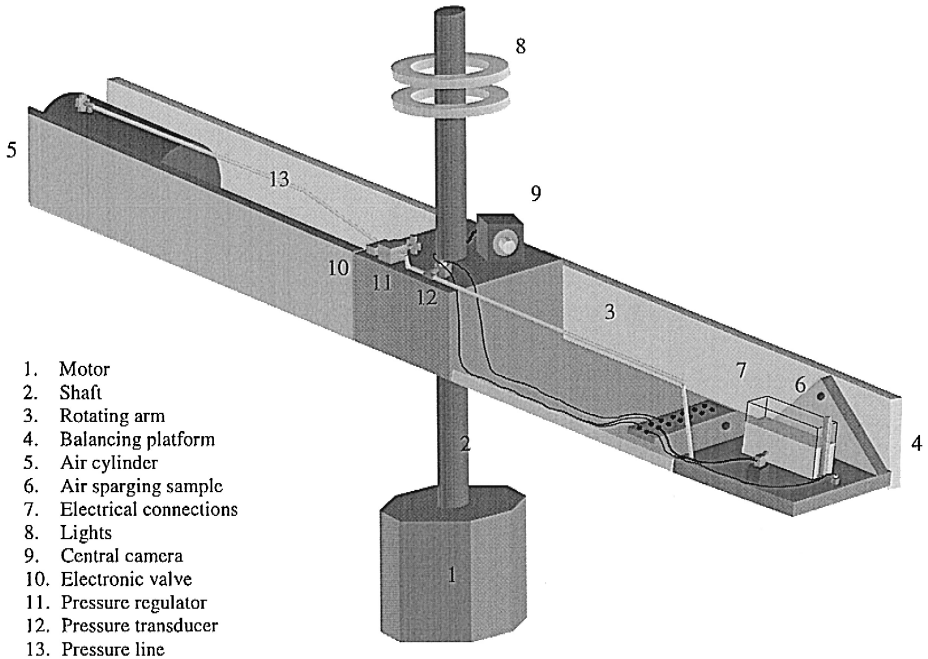13. Pressure line

Fig. 7. Diagram of geotechnical centrifuge.

1. Centrifuge platform
2. Air sparging sample
3. Air sparging plume
4. Light rack
5. Mini-camera
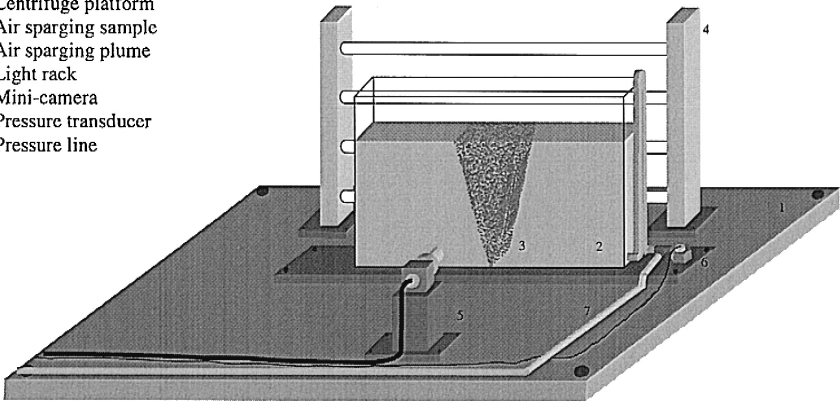6. Pressure transducer
7. Pressure line

Fig. 8. Diagram of air sparging model.

injection line. An electronic valve was also located next to the cylinder, which could be opened from the control room once the *g*-level at which injection was to take place had been reached.

Air was injected into the box through replaceable injection ports located in the center of the base of the box. Six different injection port geometries were tested, and results from all injectors are included in this paper. Injectors consist of 2 cm high brass fittings that can be screwed on to the base of the box. Two types of port geometries were tested, as depicted in Fig. 9: (1) multiple port injector (MPI) present four rows of 12 equally spaced circular orifices around the sides of the fitting; and (2) single port injector (SPI)
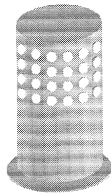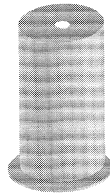
Multiple Port Injector (MPI)　　　　　Single Port Injector (SPI)

Injector Type	Injector Name	Number of Orifices	Orifice Diameter [mm]	Total Area of Injection [mm²]
MPI	Injector 1	48	2.0	150.8
MPI	Injector 2	48	1.0	37.7
MPI	Injector 3	48	0.5	9.4
SPI	Injector 4	1	2.0	3.1
SPI	Injector 5	1	1.0	0.8
SPI	Injector 6	1	0.5	0.2

Fig. 9. Characteristics of air sparging injectors.

consisting of similar fittings but with only one circular orifice on the top face. Three different orifice diameters were used for each type of injector, namely 2 mm, 1 mm and 0.5 mm. A total of six injectors were therefore used in experiments, the characteristics of which are also summarized in Fig. 9. The geometric characteristics of the injectors were chosen to facilitate comparisons with existing air injection results. SPIs were designed to be similar to orifices used in studies of bubble flow in pure liquids, such that comparisons between flow through pure liquids and flow through saturated porous media could be made. MPIs were designed as a simplified version of injection screens typically used in field applications.

7.4. Sample preparation

The crushed glass was thoroughly washed and dried before the beginning of a series of tests. The strong box was then filled with glass and vigorously shaken for approximately 5 min. The most critical factor in sample preparation was to ensure that all air had been evacuated before the box was filled with the pore fluid. Residual air bubbles trapped in the glass could create differential flow pathways through the soil, or could limit visibility once air injection started. The box was therefore covered and subjected to a vacuum (30 in. of Hg) for an hour before saturation began. Wetting was performed by opening a valve at the base of the box and by allowing pore fluid to flow upward during saturation. Any possible entrapped air bubble that might have been left after evacuation was displaced during saturation. The vacuum was left on the box for 2 h after wetting was completed. The sample was finally weighed and the phreatic surface was measured prior to testing. Sample porosity was calculated from the known weights of glass and fluid used. Finally, a grid was placed over the front face of the box that was used to track the movement of the air plume during sparging.

After the completion of each sparging test the sample was completely drained by applying a vacuum at the base of the box. The glass was then thoroughly mixed and "reworked" inside the box using a metal rod, making sure that all existing circulation channels were destroyed. The material was then densified and the evacuation/saturation procedure described above was repeated.

This paper presents results of tests performed on homogeneous samples only. Although visualization studies have been performed on heterogeneous samples, those data will not be discussed here. The coarser material was used for all tests, (i.e., $D_{10} = 0.8$ mm). All samples were prepared such that the phreatic surface was located approximately 3 to 4 cm below the top of the sample.

7.5. Experimental procedure

The operation of the centrifuge is computer-controlled from a neighboring control room. Prior to testing, an acceleration sequence was programmed in the central centrifuge computer, in which rates of acceleration and holding periods at each specific acceleration were specified. Spinning of the box under centrifugal acceleration would begin once the data acquisition system and the video recording unit had been started. At

this time, a digital chronometer was initialized and superimposed on the images being recorded. This timer was used to calculate air flow velocities through the sample.

Injection pressures were set prior to initializing the centrifugal motion and could not be adjusted during experiments. For this reason, the centrifuge was programmed to reach an acceleration slightly higher than that at which sparging was to initiate. The centrifuge was then programmed to decelerate at a very slow rate, maintaining long holding periods in between ramps. The electronic valve was opened once deceleration started, such that the exact acceleration and pressure at which breakthrough occurred could be recorded. The valve was maintained open until steady-state conditions were reached, defined here as the point at which the shape of the plume ceased to change.

Once the experiment was completed, air flow velocities and plume dimensions were obtained from recorded images. Images were played frame by frame and the displacement of the leading edge of the advancing air front was measured as a function of time. Air flow velocities were then obtained from the slopes of the plots of displacement vs. time. Digitized images were subsequently used to determine various plume characteristics such as area and rate of growth. Image analysis was performed on a personal computer using the public domain NIH Image program written by Wayne Rasband at the US National Institutes of Health and available from the Internet by anonymous FTP from zippy.nimh.nih.com.

8. Results

Results presented in this paper will only cover experiments performed using the fused silica solution (immersion fluid) as pore fluid. Equivalent tests are currently being conducted using glycerol, but the test series has not yet been completed.

8.1. Free field

Prior to conducting air sparging experiments through the saturated glass, centrifuge air injections were performed in the free field (i.e., fluid only). Tests were conducted at the same *g*-levels and with the same injectors as would later be used for the porous media injections.

8.1.1. Breakthrough velocities

As was discussed in previous sections, the use of dimensionless parameters will allow the characterization of air flow patterns during air sparging. Information on the velocity of the air breakthrough front is necessary for the calculation of the dimensionless parameters that characterize a given system. Breakthrough velocities in pure liquids and through saturated porous media will be presented, in order to evaluate the effect of the presence of the porous medium.

Free field velocities in the free field, from tests conducted using the six different injectors, were determined, and it was found that velocities in the pure liquids were uniform. Results from all injectors showed that free field velocities increased with increasing *g*-level. However, the type of injector did not have a significant effect of the

free field velocity at a specific g-level. Fig. 10 is a summary plot of the free-field velocity results as a function of g-level, where g-level refers to the value of the scaling factor n introduced in Section 6.1.

8.1.2. Flow patterns

Air flow patterns observed in the free field are consistent with observations presented in Section 4.1. At low g-levels, bubbles injected from SPIs rise independently and their trajectory is rectilinear. As the g-level increases and exceeds $30 \times g$, the size of the bubbles from injectors 4 (SPI, $D = 2$ mm) and 5 (SPI, $D = 1$ mm) increases during their ascent. Bubble trajectory continues to be primarily rectilinear, but lateral deviations from the vertical path are observed. Other than an increase in velocity, the general behavior of bubbles from injector 6 (SPI, $D = 0.5$ mm) is relatively unaffected by the increasing acceleration. At g-levels higher than $60 \times g$ bubble coalescence occurs as the bubbles rise. Coalescence leads to the formation of considerably larger bubbles and to a large number of very fine bubbles. Liquid recirculation patterns become evident as ''slushing'' occurs against the sides of the box.

The behavior of bubbles injected from MPIs differs slightly. Multiple bubbles enter the box at the same time, and establish a liquid circulation pattern close to the injector. Bubbles rise with a swirling motion and tend to collide with each other, therefore
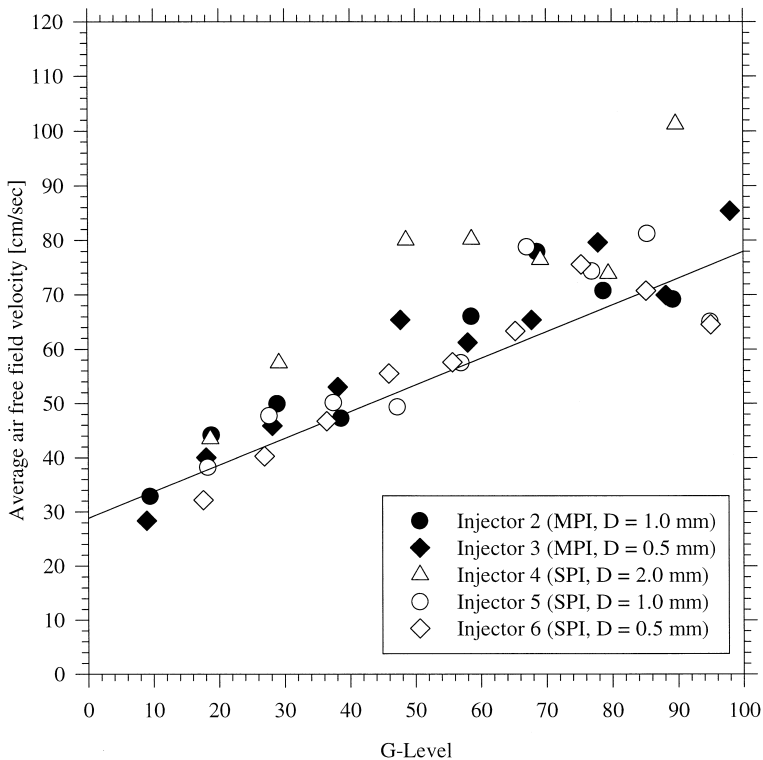

Fig. 10. Free field velocities vs. g-level during centrifuge tests.

creating turbulent conditions at lower g-levels than those observed for single opening ports. This condition is accentuated for bubbles produced by injectors 1 (MPI, $D = 2$ mm) and 2 (MPI, $D = 1$ mm), which increase in size during ascent.

8.2. Porous media

8.2.1. Breakthrough velocities

Fig. 11(a) through (f) presents a summary of experimental results obtained from sparging tests. Refer to Table 2 for a summary of the controlling dimensionless numbers
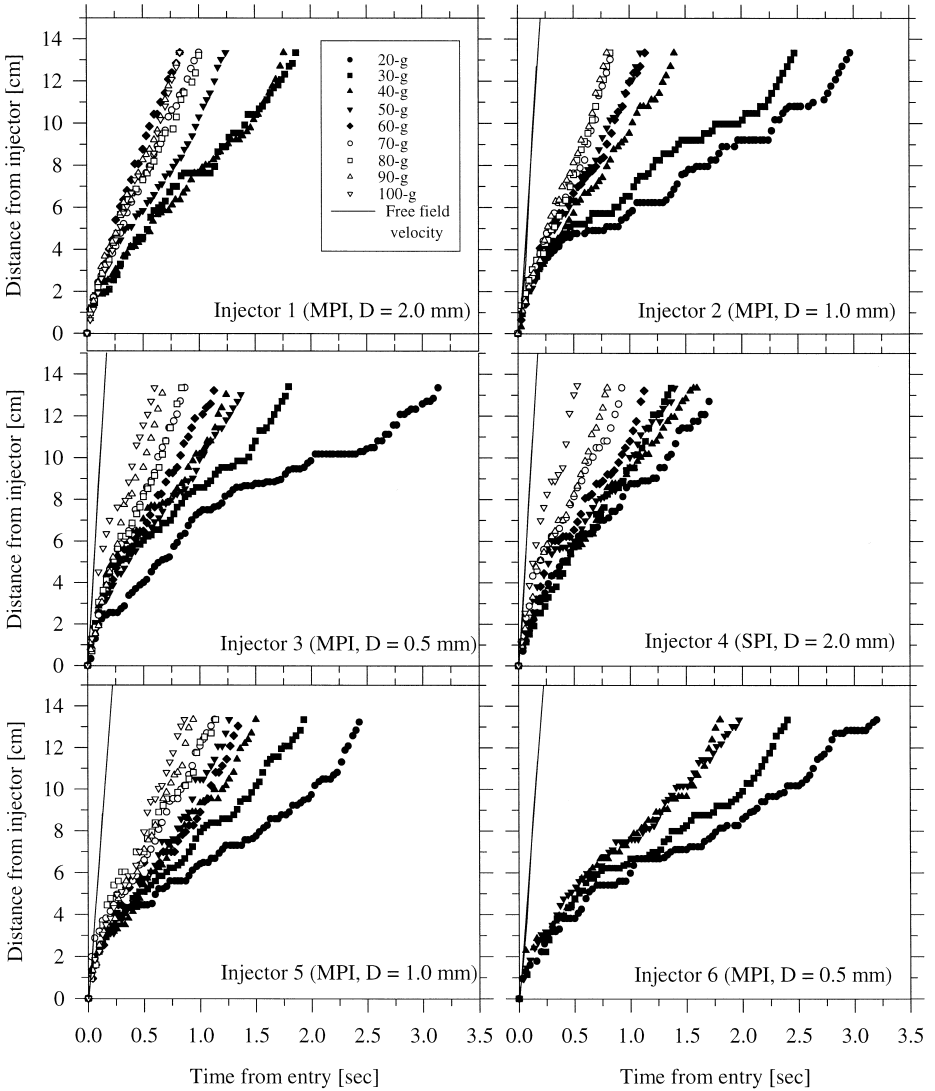

Fig. 11. Displacement vs. time at varying g-level during centrifuge tests.

Table 2
Air flow velocities and dimensionless numbers of air sparging tests

g-level	Breakthrough velocity [cm/s]	Re	Bo	$Ca \times 10^2$	We
50	8.95	3.41	8.88	5.33	0.18
60	10.03	3.82	10.66	5.97	0.23
70	12.14	4.63	12.43	7.22	0.33
80	12.19	4.64	14.21	7.25	0.34
90	14.15	5.39	15.99	8.42	0.45
100	14.61	5.56	17.76	8.69	0.48

for these results. The vertical distance from the top of the injector to the leading edge of the advancing plume is plotted as a function of the time at which breakthrough starts. In essence, these graphs show the advancement of the breakthrough front from the moment it enters the porous medium to the moment it leaves the field of vision of the mini-camera. The slope of these plots is therefore the velocity of the injected air. Six graphs are included on the figure, each summarizing results obtained from one specific injector (injectors 1–6). Within each plot, each curve shows results from one test conducted at a specific g-level. Included for reference in each graph is also a plot of the free field velocity.

As shown by Fig. 11 the breakthrough velocity of the air plume increases with increasing g-level, for all injectors. This result was expected, since injection pressures for these tests were set equal to the minimum injection pressure and from Eq. (8), $(P_{inj})_{min}$ increases with g. Breakthrough velocities however are not uniform at all g-levels, and non-uniformity increases with decreasing injector opening size. Breakthrough velocities for experiments conducted at accelerations equal to $50 \times g$ and higher are uniform for all injectors. At lower accelerations, breakthrough velocities are significantly lower and non-uniform. Below $40 \times g$, the advancement of the plume is arrested after a certain distance, which decreases with decreasing g-level. The plume stops moving forward and it either spreads laterally or remains of constant size, resulting in a step-like plot. At this time, the distance from the injection port determines the behavior of the plume during its arrest: if the front is stopped close to the injector, marginal lateral growth of the plume takes place, most likely due to the fact that the hydrostatic pressure remains high. As the distance from the injector increases, and therefore the hydrostatic pressure decreases, lateral spread of the plume becomes more pronounced.

Average velocities of experiments over $50 \times g$ from all injectors were grouped by g-level as shown in Fig. 12(a) through (f), and results are summarized in Table 2. It is clear that at accelerations higher than $60 \times g$ neither the opening size of the injector nor its geometry has any effect on the breakthrough velocity of the injected air. Reynolds numbers for the flow at breakthrough range from 3.4 to 5.6. If the boundaries for single-phase flow through porous media determined by Wright [11] are used as a reference, this region of flow corresponds to the transition between laminar and steady inertial flow.

Linearized free field velocities (v_{FF}) and average breakthrough velocities for all injectors (v_{ave}) for experiments conducted at g-levels higher than $50 \times g$ are plotted as a
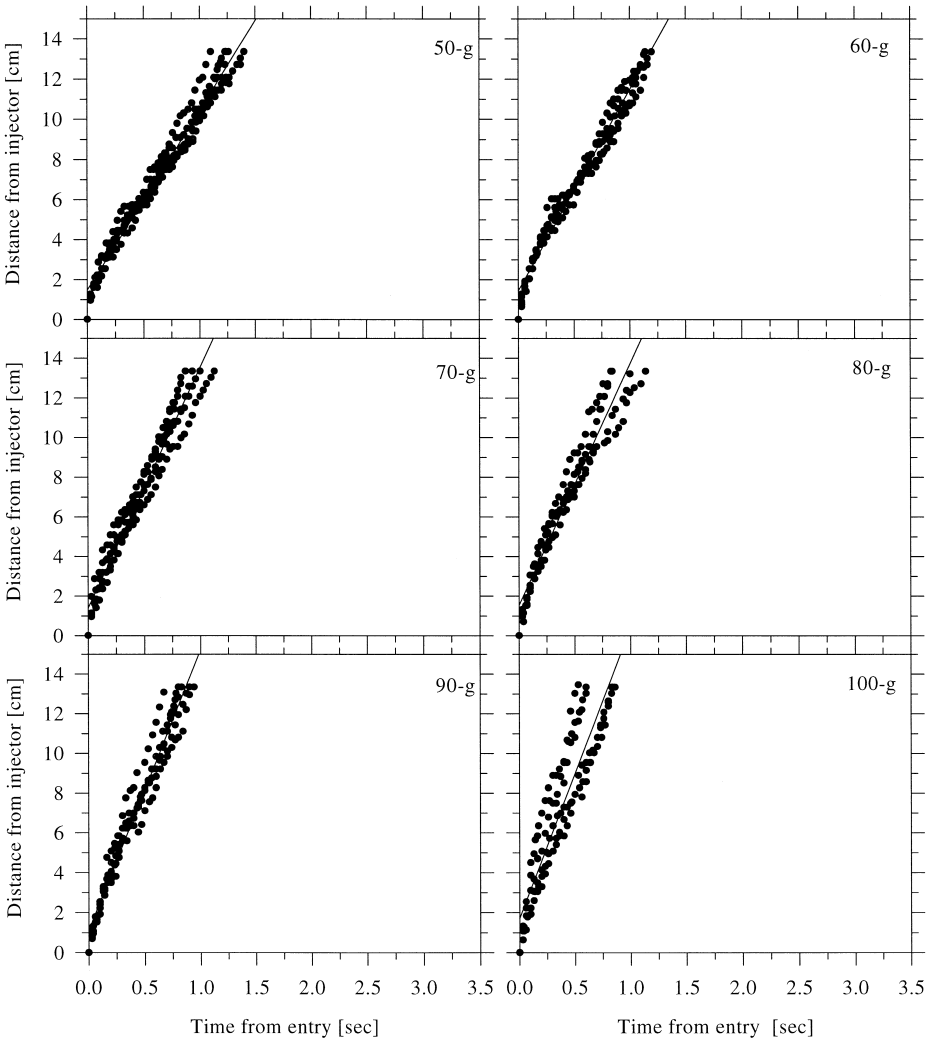
Fig. 12. Linearized displacement vs. time plots.

function of g-level on Fig. 13(a) and (b). Fig. 13(c) shows a plot of the ratio v_{FF}/v also as a function of acceleration. Although there is a slight decrease in the value of v_{FF}/v with increasing g-level, for accelerations ranging from $50 \times g$ to $100 \times g$, velocities of the air through the porous medium are approximately six times smaller than those in the free liquid.

8.2.2. Plume shapes

One of the largest uncertainties left to clarify in the study of air sparging, concerns the size of the zone of influence of a sparging well. The use of various injection pressures and injector geometries was planned such that this question could be ad-
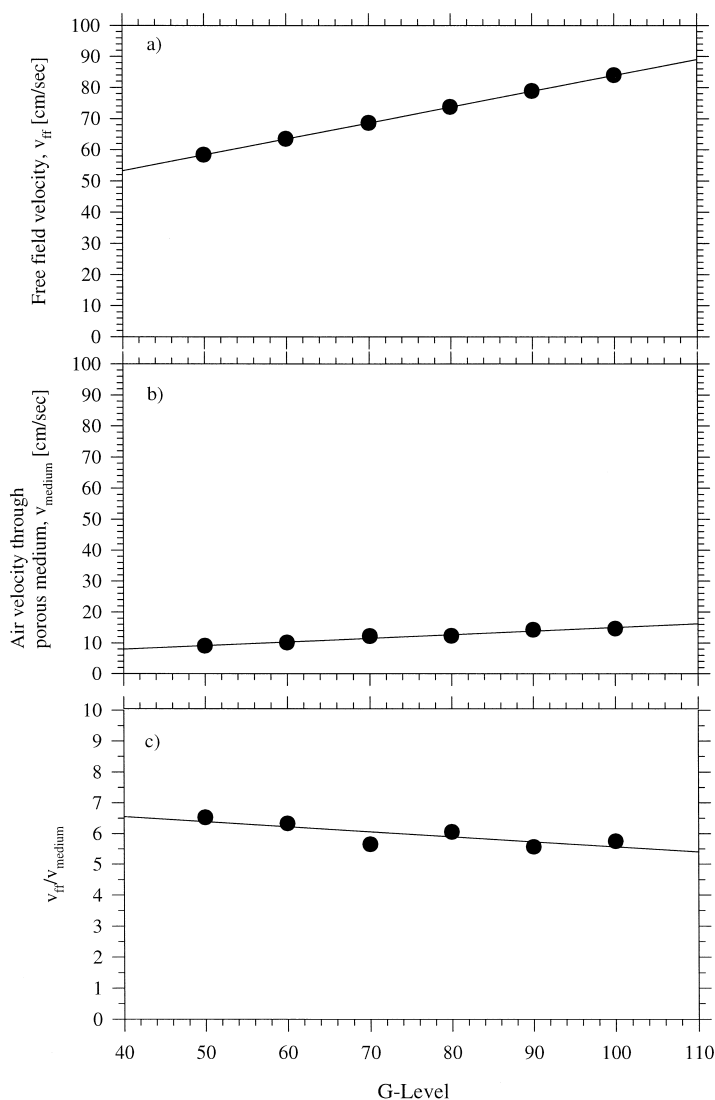
Fig. 13. Linearized free field and breakthrough velocities at high *g*-levels.

dressed. Figs. 14–17 include pictures of steady-state air plumes taken during centrifuge air sparging experiments in fused silica solution. There is a clear difference between the plumes formed at lower *g*-level and those that develop at higher accelerations. Channel density of the air plumes formed at *g*-levels ranging from $10 \times g$ to $30 \times g$, estimated from color scheme intensity, is lower than that of plumes at higher *g*-levels. Low-*g* plumes are not as well delineated, and the interface between the liquid-saturated and the air-saturated regions is not sharp. Zones of intermediate air saturation values exist in the low-*g* plumes but are not present around the edges of the high-*g* plumes. Both of these
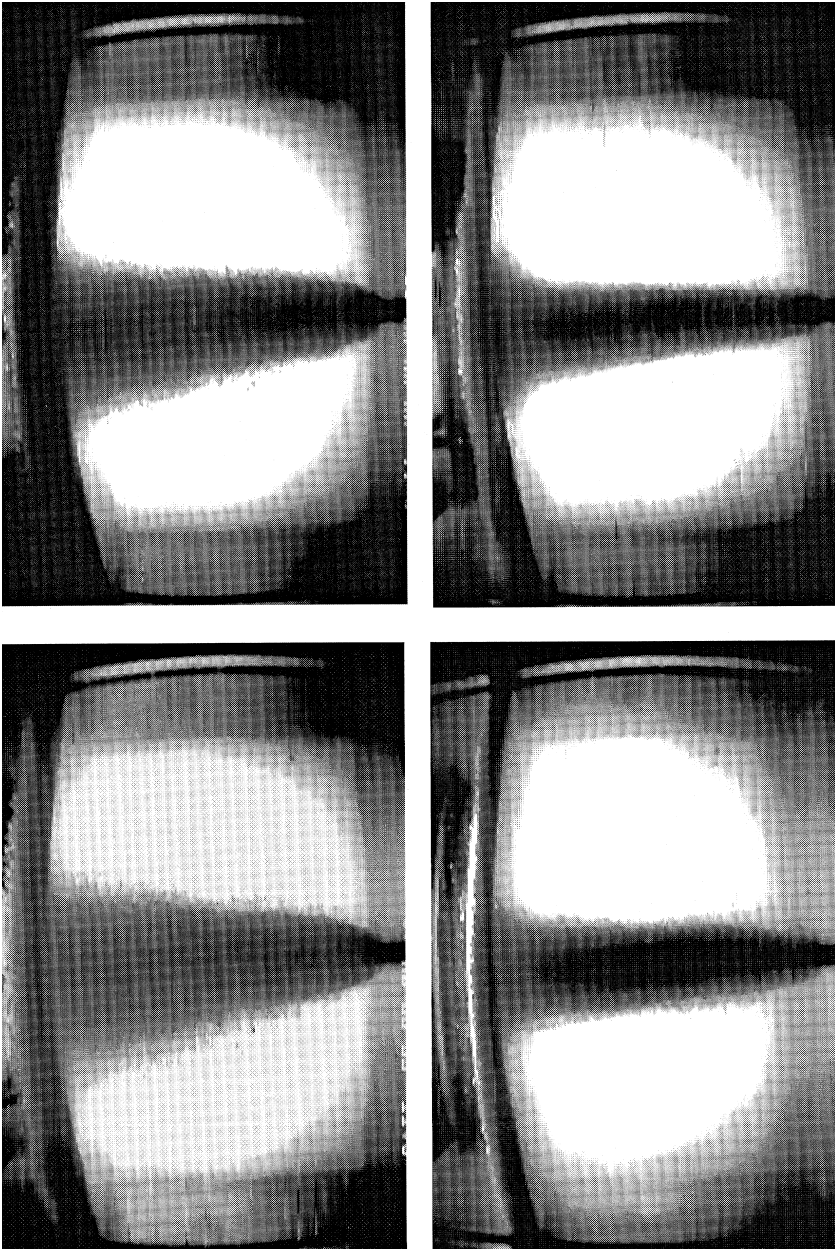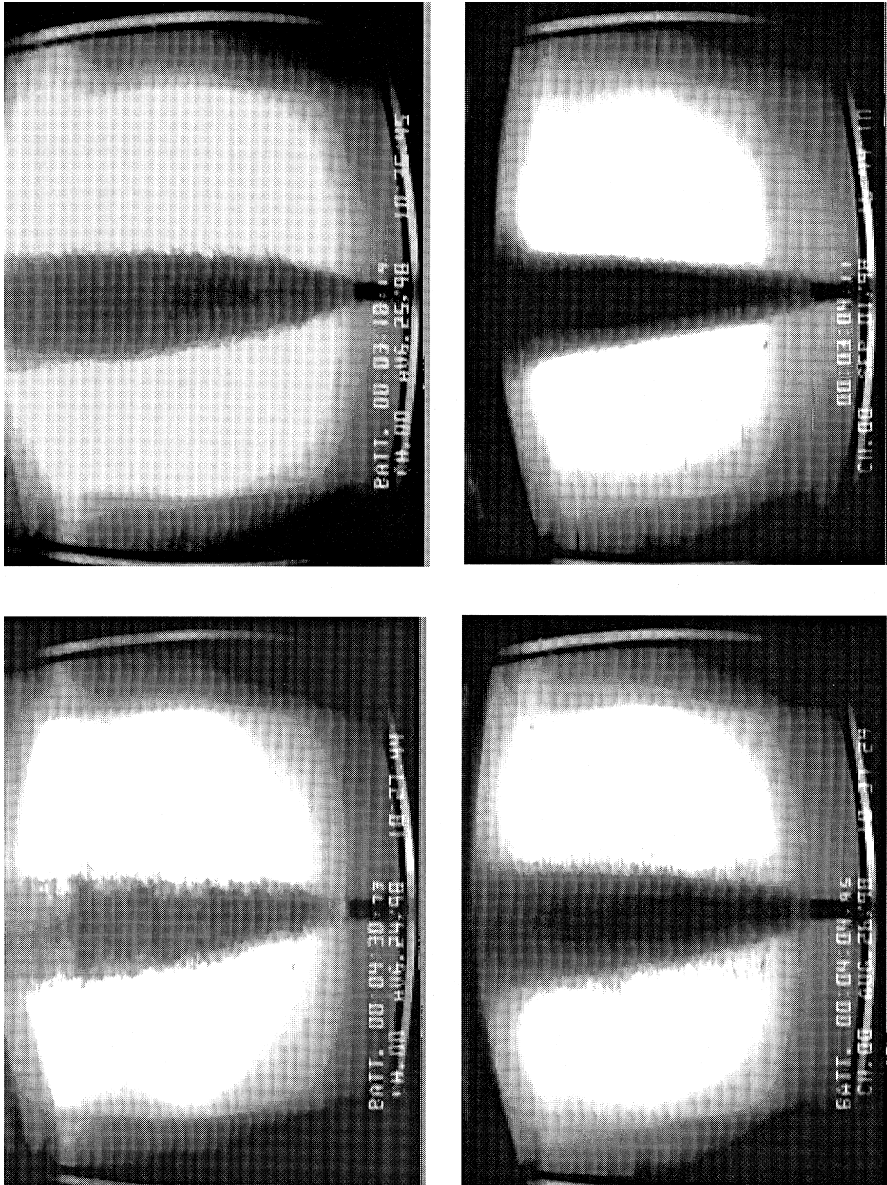
Fig. 14. Air plumes — injector 1.
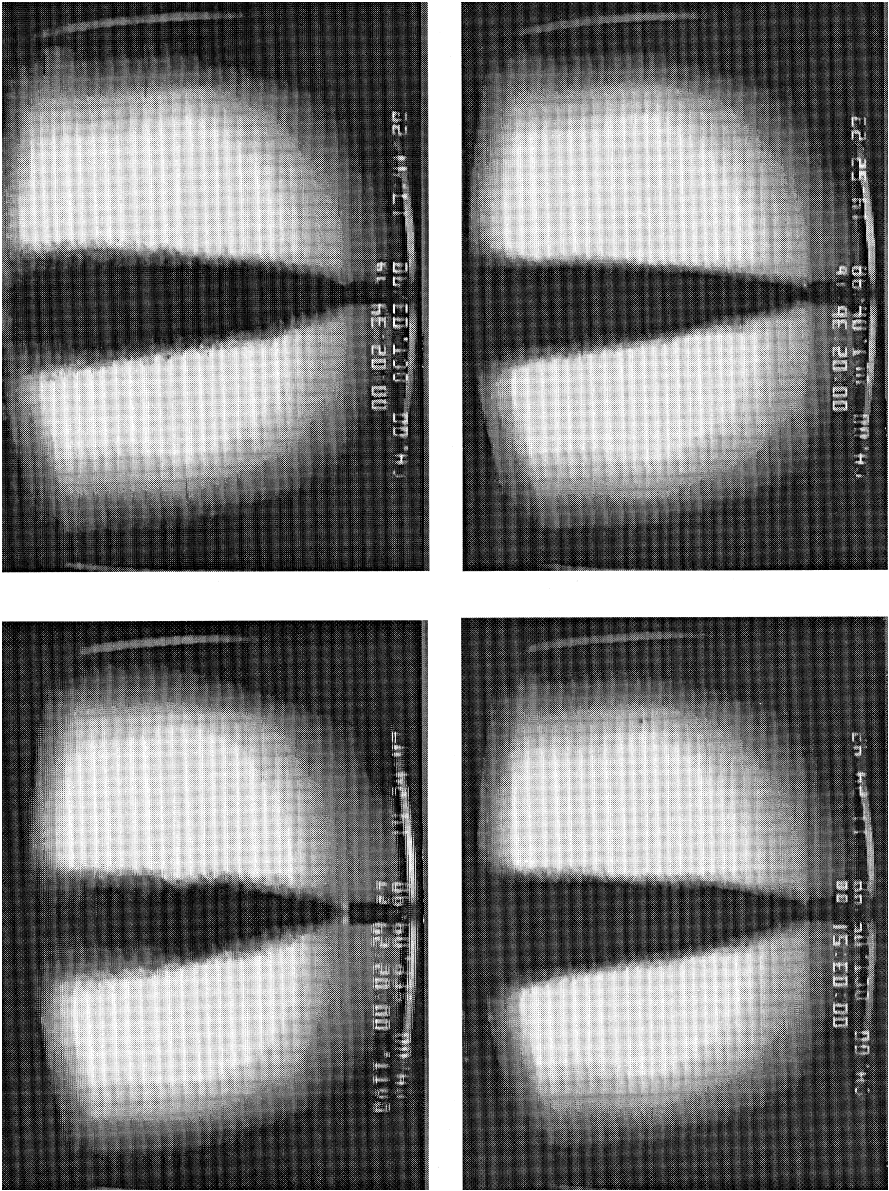
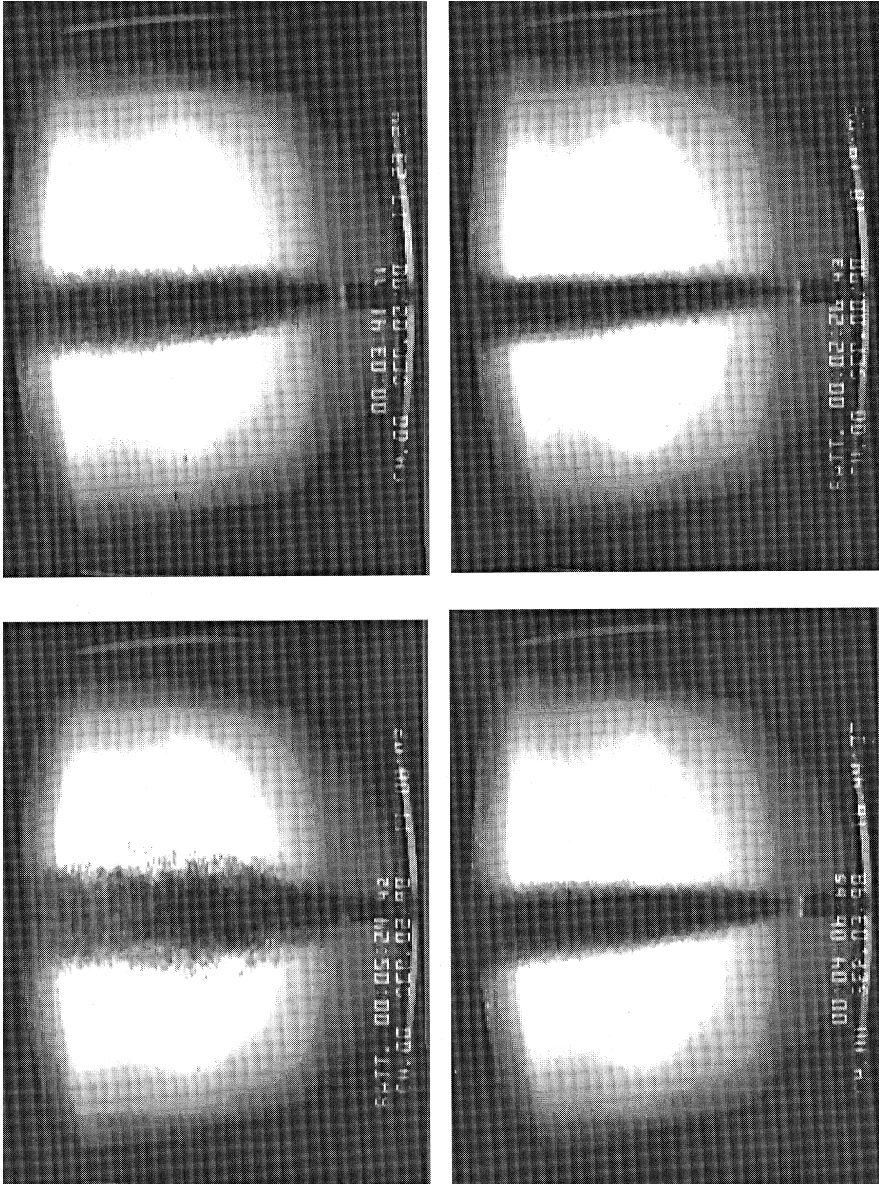Fig. 15. Air plumes — injector 3.

Fig. 16. Air plumes — injector 4.

Fig. 17. Air plumes — injector 6.

observations are consistent with the velocities measured during experiments. At lower accelerations air flow is not continuous and it periodically spreads in the horizontal direction. Temporary flow pathways are created, but the bulk of the flow will move upward when the invading front continues to advance.

The shape of the plumes is conical, as expected. The angle of inclination of the sides however, is not exclusively related to the soil type as indicated by Nyer and Sutherson [3], since it varies between images. The geometry of the injector has a definite impact at the apex of the cone. Plumes produced from single opening injectors are clearly differentiated by the steep inclination of their sides, while plumes resulting from multiple opening injectors are wider at their base.

The factors controlling the extent of the zone of influence are still not fully established. It is clear from the experimental images collected, that increasing g-level, and therefore injection pressure, leads to a decreasing zone of influence. However, the relationship between pressure and area of plume is not always consistent from injector to injector. It can also be stated that both the total area of injection and the geometry of the injection port significantly affect the final area of the air plume, as seen by comparing pictures from injectors 4 and 6 (SPI, $D = 2$ mm and $D = 0.5$ mm, respectively). These differences in zone of influence are not consistent though, as no significant differences were measured between zone of influence resulting from injectors 1 and 3, and from injectors 4 and 6.

8.2.3. Observed flow conditions after breakthrough

Once the advancing air front fully breaks through and reaches the phreatic surface of the sample, flow conditions visibly change. No air flow velocities for this stage of the tests are available, since the method used to determine velocities during invasion is no longer applicable. Once the initial air plume has invaded the medium, the contrast between air and saturated soil no longer exists and air transport cannot be accurately tracked. However, the behavior of the entire plume changes and pulsing becomes apparent. Pulsing is used here to describe a mode during which the zone of influence of the injector does not vary, but periodic oscillations of the edges of the plume occur. The air plume essentially contracts and expands in place. Pulsing occurs at all g-levels, but becomes increasingly pronounced with increasing injection pressure.

8.3. Discussion of results

8.3.1. Free field

Bubble patterns observed in the free field are consistent with those quoted in the literature. The system is very turbulent, even at low g-levels, and bubble geometry can therefore not be estimated. There is no consistent trend between air flow velocity in the free field and port opening size for experiments conducted in the fused silica fluid. Average free field velocities appear to be relatively independent of injector size, and increase with increasing g-level.

8.3.2. Porous media

Pore size, and consequently soil type, does not *exclusively* control the flow of air through saturated porous media at g-levels lower than $50 \times g$. Injector geometry has a

definite effect on air velocity through the porous medium. Results for single opening injectors show that air velocities decrease with decreasing port opening.

Velocities at low g-levels for single opening injectors are not uniform. Air flow through the medium occurs in stages: the air plume advances predominantly in the vertical direction until breakthrough stops. Lateral growth of the plume then occurs, until sufficient pressure builds up to cause a new breakthrough. This process is repeated several times during the same experiment, inducing lateral spreading and therefore growth of the zone of influence of the plume. For single opening injectors, the number of stages increases with decreasing port opening size.

At accelerations higher than $50 \times g$, the geometry of the injection port does not appear to control the resulting air flow velocity through the porous medium. Velocities increase with increasing g-level, but their magnitude is not dependent on the size of the port openings. At these high accelerations, breakthrough velocities are proportional to free field velocities.

A hypothesis of air flow through saturated porous media can be formulated by combining the results presented with the theory included in earlier sections. The flow of air through homogeneous porous media resulting from air sparging operations is inherently unstable, as stated by Eq. (4). At low g-levels, fingering occurs during the initial phase injection, as air displaces the existent pore fluid, under laminar flow conditions. Laminar flow conditions prevail at low g-levels, given that the flow rate is relatively low and that the frequency of bubble emission is not sufficiently high to create turbulent conditions. The scale of the fingers is in the order of the medium pore size, and therefore no dominant fingers are formed. Air is introduced into the medium in the form of discrete bubbles, but capillary constraints are encountered immediately upon exiting the injector, given that only limited pore space is available for flow. Bubbles coalesce outside the orifice, increasing the pressure that drives the fingers. The observed patterns of flow at low g-levels for the experiments reported here are indeed consistent with fingering flow: the leading edge of the air front has a non-uniform velocity and spreads both laterally and horizontally until it reaches the phreatic surface.

As injection flow rate is increased the frequency of bubble emission increases, the driving pressure behind the front becomes significant, and the breakthrough front advances at high velocity. The flow regime becomes turbulent at this stage, and the water table is quickly reached. At this point, interconnected channels develop from the injector to the water table and the flow regime changes again. Observations of pulsing flow are consistent with descriptions of slug or annular flow.

9. Conclusions

This paper has presented results of experiments conducted to study the mechanisms controlling the flow of air through saturated porous media during air sparging. Experiments have been conducted in a geotechnical centrifuge, under a wide range of gravitational accelerations. Results show that air flow patterns vary from fingering, at low g-levels, to pulsing at higher accelerations. Grain and pore size distribution of the porous medium do not exclusively control air flow characteristics. Injector geometry has

a definite effect on breakthrough velocities and air plume shapes. Experiments have been conducted to compare the velocity of air flow through the saturated porous medium to that of air in pure liquids. Results show that the velocity of air though the medium is lower than that in the pure fluid, as expected. At high *g*-levels however, plume breakthrough velocities are proportional to the velocity of the air in the pure fluid.

Acknowledgements

References

[1] H. Widjaja, J.M. Duncan, H.B. Seed, Scale and Time Effects in Hydraulic Fracturing, US Army Corps of Engineers, Miscellaneous Paper GL-84-10, 1984, p. 192.

[2] T.W. Lambe, R.V. Whitman, Soil Mechanics, Wiley, New York, 1969, p. 545.

[3] E.K. Nyer, S.S. Sutherson, GWMR 13 (4) (1993) 87.

[4] K.R. Reddy, S. Kosgi, J. Zhou, Hazard. Waste Hazard. Mater. 12 (2) (1995) 97.

[5] M.R. Chen, R.E. Hinkley, J.E. Killough, Water Resour. Res. 32 (10) (1996) 3013.

[6] P.D. Lundegard, G. Andersen, Proc. of the 1993 Petroleum Hydrocarbons and Organic Chemicals in Ground Water: Prevention, Detection, and Restoration, Houston, TX, 1993, 461.

[7] R.A. Wooding, H.J. Morel-Seytoux, Annu. Rev. Fluid Mech. 8 (1976) 233.

[8] P.J. Culligan, D.A. Barry, Proc. Inst. Civ. Eng. Geotech. Eng. 131 (1998) 180.

[9] S. Ratnam, P.J. Culligan-Hensley, J.T. Germaine, Proc. of the Second International Congress on Environmental Geotechnics, Osaka, Japan, 1996, 1061.

[10] J.R. Grace, T. Wairegi, T.H. Nguyen, Trans. Inst. Chem. Eng. 54 (1976) 167.

[11] D.E. Wright, Proc. Am. Soc. Civ. Eng. 94 (HY4) (1968) 851.

[12] G.M. Homsy, Annu. Rev. Fluid Mech. 19 (1987) 271.

[13] S. Hill, Chem. Eng. Sci. 1 (6) (1952) 247.

[14] S.P. Gupta, R.A. Greenkorn, Water Resour. Res. 10 (2) (1974) 371.

[15] B.H. Kueper, E.O. Frind, J. Contam. Hydrol. 2 (1988) 95.

[16] D. Pavone, SPE Reservoir Eng. May (1992) 187.

[17] J.P. Stokes, D.A. Weitz, J.P. Gollub, A. Dougherty, M.O. Robbins, P.M. Chaikin, H.M. Lindsay, Phys. Rev. Lett. 57 (14) (1986) 1718.

[18] D.C. Brock, F.M.J. Orr, Proc. 66th SPE Annual Technical Conference and Exhibition, Dallas, TX, Gamma, 1991, 211.

[19] C.T. Tan, G.M. Homsy, Phys. Fluids 4 (6) (1992) 1099.

[20] U.G. Araktingi, F.M.J. Orr, SPE Adv. Technol. Ser. 1 (1) (1993) 71.

[21] D.E. Moissis, M.F. Wheeler, C.A. Miller, SPE Adv. Technol. Ser. 1 (1) (1993) 62.

[22] A.B. Ponter, A.I. Surati, Chem. Eng. Technol. 20 (1997) 85.

[23] D.W. Van Krevelen, P.J. Hoftijzer, Chem. Eng. Prog. 46 (1) (1950) 29.

[24] R.R. Hughes, A.E. Handlos, H.D. Evans, R.L. Maycock, Chem. Eng. Prog. 51 (12) (1955) 557.

[25] L. Davidson, E.H.J. Amick, AIChE J. 2 (3) (1956) 337.

[26] I. Leibson, E.G. Holcomb, A.G. Cacoso, I.J. Jacmic, AIChE J. 2 (3) (1956) 296.

[27] W.L. Haberman, R.K. Morton, Trans. ASCE 121 (1956) 227.
[28] G.B. Wallis, One-dimensional Two-phase Flow, McGraw-Hill, New York, 1969, p. 408.
[29] R. Clift, J.R. Grace, M.E. Weber, Bubbles, Drops, and Particles, Academic Press, New York, 1978, p. 351.
[30] V.G. Levich, Physicochemical Hydrodynamics, Prentice Hall, 1962, p. 700.
[31] P.P. Wegener, J.Y. Parlange, Annu. Rev. Fluid Mech. 5 (1973) 79.
[32] G.B. Wallis, Int. J. Multiphase Flow 1 (1974) 491.
[33] R. Comolet, Houille Blanche 34 (1) (1979) 31.
[34] R. Comolet, J. Mec. Appl. 3 (2) (1979) 145.
[35] Y. Taitel, D. Bornea, A.E. Dukler, AIChE J. 26 (3) (1980) 345.
[36] K. Mishima, T. Hibiki, Int. J. Multiphase Flow 22 (4) (1996) 703.
[37] M. Fourar, S. Bories, Int. J. Multiphase Flow 21 (4) (1995) 621.
[38] J.F. Davidson, D. Harrison, J.R.F. Guedes de Carvalho, Annu. Rev. Fluid Mech. 9 (1977) 55.
[39] K. Tsuchiya, G.H. Song, L.S. Fan, Chem. Eng. Sci. 45 (5) (1990) 1429.
[40] M.J. Bly, R.M. Worden, Chem. Eng. Sci. 47 (13/14) (1992) 3281.
[41] K. Tsuchiya, A. Furumoto, AIChE J. 41 (6) (1995) 1368.
[42] J.L. Turpin, R.L. Huntington, AIChE J. 13 (6) (1967) 1196.
[43] V.W.J. Weekman, J.E. Myers, AIChE J. 10 (6) (1964) 951.
[44] S.P. Gido, D.E. Hirt, S.M. Montgomery, R.K. Prud'homme, L. Rebenfeld, J. Dispersion Sci. Technol. 10 (6) (1989) 785.
[45] C.W. Nutt, R.W. Burley, D.M. Anwer Rajah, J.T. Polychronopolis, Int. J. Eng. Fluid Mech. 5 (3) (1992) 373.
[46] W. Ji, A. Dahmani, D.P. Ahlfeld, J.D. Lin, E. Hill, GWMR 13 (4) (1993) 115.
[47] K. Wehrle, Proc. Contaminated Soil'90, Third International KfK/TNO Conference on Contaminated Soil, 1990.
[48] R. Semer, J.A. Adams, K.R. Reddy, Geotech. Geol. Eng. 16 (1998) 59.
[49] D.M. Baker, C.H. Benson, Proc. of the Specialty Conference on Non-Aqueous Phase Liquids (NAPLs) in Subsurface Environment — Assessment and Remediation, Washington, DC, 1996, 292.
[50] U. Bohler, J. Brauns, M. Nahold, Contaminated Soil'90, Third International KfK/TNO Conference on Contaminated Soil 2, 1990, 103.
[51] M.C. Marley, D.J. Hazebrouck, M.T. Walsh, GWMR 12 (2) (1992) 137.
[52] K. Arulanandan, P.Y. Thompson, B.L. Kutter, N.J. Meegoda, K.K. Muraleetharan, C. Yogachandran, J. Geotech. Eng. 114 (2) (1988) 185.
[53] P.J. Hensley, C. Savvidou, Aust. Geomech. 22 (1992) 7.
[54] R.N. Taylor, Geotechnical Centrifuge Technology, Blackie Academic and Professional, Glasgow, 1995, p. 296.
[55] D.P. Ahlfeld, D. Amine, J. Wei, Ground Water Monit. Rev. 14 (4) (1994) 132.
[56] R. Brown, Handbook of Bioremediation, Lewis Publishers, Boca Raton, 1995, p. 257.
[57] T. Wakabayashi, J. Phys. Soc. Jpn. 35 (2) (1950) 383.
[58] P. Dantu, Proc. Int. Conf. Soil Mech. Found. Eng. 1 (1957) 144, London.
[59] P. Rangelow, K. Konagai, T. Matsushima, C.S. Park, Bull. ERS 25 (1992) 61.
[60] K. Konagai, C. Tamura, P. Rangelow, T. Matsushima, Struct. Eng./Earthquake Eng. 9 (3) (1992) 193s.
[61] C.D. Montemagno, W.G. Gray, Geophys. Res. Lett. 22 (4) (1995) 425.
[62] A. Pahwa, MS Thesis, Dept. Civil and Environmental Eng., MIT, 1987, p. 199.